machines

MDPI

Article

Beyond Linear Limits: Advanced Nonlinear Suspensions for Enhanced Vibration Control

Farhad S. Samani [1], Amirali Mehrabian [1], Antonio Zippo [2,*] and Francesco Pellicano [2]

[1] Department of Mechanical Engineering, Shahid Bahonar University of Kerman, Kerman 76169-14111, Iran; farhad.samani@uk.ac.ir (F.S.S.); amirali.mehrabian.81@gmail.com (A.M.)
[2] Department of Engineering "Enzo Ferrari", Centre InterMech MoRe, University of Modena and Reggio Emilia, 41125 Modena, Italy; francesco.pellicano@unimore.it
* Correspondence: antonio.zippo@unimore.it

Abstract

The vehicle suspensions have the primary task of attenuating the forces coming from the road surface. The performance is directly linked to the stiffness of the suspension system. Traditional suspensions, composed of linear elements, effectively damp high frequencies but perform poorly at low frequencies. In this regard, non-linear suspensions, characterized by a non-linear force–displacement relationship, have been introduced. These types of suspensions achieve this characteristic by combining elements with positive stiffness with elements with negative stiffness, resulting in an equivalent system with quasi-zero stiffness (QZS) around the equilibrium. The performance of the QZS suspension system is analyzed here using the Multibody Dynamics software MSC Adams® (2022.2). Static characteristics, transmissibility, and isolation performance are investigated through dynamic tests based on road profiles according to ISO 8608 regulations generated using MATLAB® (R2022b). The proposed quasi-zero stiffness suspension demonstrates an improvement of approximately 19% in vibration attenuation compared to a conventional suspension system under realistic road excitations.

Keywords: quasi-zero stiffness; non-linear suspension; primary vehicle suspension; multibody dynamics; vibration isolation; ride comfort; ISO 8608

1. Introduction

The increasing needs of high-precision tooling, e.g., in automotives, electronics, or aerospace, in extreme working environments have led to a special need for low- and ultra-low-frequency vibration isolation systems. Traditional linear isolators face challenges when attempting to mitigate vibrations at low frequencies without compromising system stability. To address this issue, non-linear isolators, specifically Quasi-Zero Stiffness (QZS) isolators, have been proposed. These isolators achieve almost zero stiffness through combining positive and negative stiffness mechanisms. QZS isolators effectively decrease vibrations at low frequencies, support high static loads, and maintain system stability. Their applications cover diverse fields, including isolating ship instrumentation, reducing loads during aerospace launches, mitigating impact-induced vibrations, safeguarding structures from earthquakes, and protecting various systems and occupants from ground-induced and machinery vibrations. In the design of QZS mechanisms, the primary goal is to balance positive stiffness with negative stiffness elements, utilizing passive, active, or semi-active methodologies. Vibration isolation systems use various passive mechanisms

Academic Editor: Walter D'Ambrogio

Received: 22 December 2025
Revised: 2 February 2026
Accepted: 5 February 2026
Published: 10 February 2026

such as mechanical springs, flexural beams, and magnetic components. Mechanical springs may introduce limitations; magnetic springs offer controlled negative stiffness and active and semi-active systems, and they utilize position feedback and adapt better to diverse conditions than passive mechanisms. QZS isolators, a passive type of system, address the contradiction in linear systems by combining positive and negative stiffness, minimizing equivalent stiffness, and enhancing mechanical isolation. In the proposed suspension architecture, the negative stiffness effect arises from the geometric arrangement of the inclined elastic elements, whose restoring force components counteract the positive stiffness contribution of the main spring. The calibrated contributions establish a working region with minimized stiffness, using force and displacement transmissibility as key criteria. The evaluation of the transmissibility of force and displacement is an important criterion in the analysis of mechanical insulation performance, and, according to classical vibration theory [1], can be written as

$$T_R = \sqrt{\frac{\left(1 + (2\zeta r)^2\right)}{\left((1 - r^2)^2 + (2\zeta r)^2\right)}} \tag{1}$$

where ζ is the damping ratio, r = ω/ω_n is the frequency ratio, ω denotes the excitation frequency, and ω_n is the natural frequency of the system.

In the QZS system, a higher frequency ratio ($r = \omega/\omega_n$, ω is the excitation and ω_n is the fundamental frequency) reduces transmissibility in the suppression region ($r > \sqrt{2}$), effectively decreasing the natural frequency and enhancing load capacity for mechanical isolation. QZS mechanisms, with their non-linearity, offer a unique advantage for achieving both reduced natural frequency and high load capacity compared to linear isolators. Displacement and force transmissibility depend on non-linearity, damping ratio, and excitation amplitude. The system's nonlinearity introduces a curvature in the amplitude–frequency relationship: for the softening systems, the higher the vibration amplitude, the lower the resonance frequency; the opposite happens for hardening systems. Two distinct regions in the amplitude–frequency response are identified, potentially leading to the jump-up or jump-down phenomenon, as detailed by Brennan et al. [2] in their investigation of Duffing oscillators using the Harmonic Balance Method. The initial QZS suspension design comprises three parallel mechanical springs: two obliques for negative stiffness and one vertical for positive stiffness [3]. Different structures, such as multi-spring, special spring, sliding block-rod, and origami, originated from the primary structure. Despite these variations, they all use linear elements to replicate the nonlinear contribution, with the specific geometric and structural configuration defining the system's nonlinear elastic response and QZS characteristic. Zhao et al. [4] proposed a multi-spring structure that can be redesigned for different applications and working conditions. It consists of three pairs of oblique springs capable of counteracting the positive stiffness contribution of the vertical spring. This structure can reduce transmissibility compared to the model with two oblique springs. Lan et al. [5] replicated the basic mechanism by reshaping the horizontal springs as planar springs to allow stiffness variation through design modifications. They also implemented manual actuators at the free ends of oblique and vertical springs for controlling the system configuration. Lateral tuning compensates for deviations in stiffness and geometric ratios, while vertical tuning maintains the mechanism operating around equilibrium under varying loads. The structure proposed by Danh Le et al. [6] is a sliding rod-type, comprising a vertical spring supporting the mass, a vertical damper, and, in parallel, two horizontal springs connected to the suspended mass through two oscillating arms. Ye et al. [7] proposed an origami structure composed of beams and springs, modeling the stiffness of origami folds. The precise selection of stiffness and geometric parameters can

yield various system responses optimized for different applications and working conditions. Applying these types of isolators exhibits a force–displacement relationship expressed as a convex function. It is crucial to limit the working range to positive equivalent stiffness values to prevent instability in the system. All these isolator structures share the characteristic of High Static Low Dynamic Stiffness, a critical feature for effectively suppressing low frequencies without losing high payload capacity. The incorporation of multi-spring structures extends the isolation range and minimizes resonance peaks. While specially designed springs can enhance effectiveness in compact and high-stiffness structures, their design poses challenges. Parameters governing stiffness and loading capacity fall into two groups: "design parameters" and "tuning parameters". Design parameters set initial constraints, while tuning parameters allow adjustments based on working conditions.

Replacing the oblique springs with buckled beams provides an equivalent elastic behavior governed by the beam's own stiffness, which can be expressed as $K_b = \pi^2 EI/L^2$, where E is the Young's modulus, I is the moment of inertia of the beam, and L is half the length of the unloaded beam. Liu et al. [8] considered a low-frequency isolator using Euler buckled beams as a negative stiffness corrector, and Huang et al. [9] applied a non-linear isolator using a double Euler buckled beam on each side.

Cam–Roller–Spring is based on the sliding and consequent compression of the elastic element, a roller on the profile of a cam. The adopted cam geometry determines the non-linearity of the force–displacement relationship that compensates for the positive stiffness contribution. Zhou et al. [10] developed a cam–roller mechanism, achieving an excellent transmissibility response and isolation performance. Later, the same authors proposed a compact design based on the same working principle: the cam–roller mechanism was integrated into a "strut" [11]. Using a tripod of these struts, they also proposed a six-degree-of-freedom platform isolator. Finally, they adapted the principle for rotary or torsional applications, proposing a QZS torsional isolator capable of attenuating vibrations transmitted between two rotating shafts [12].

Shan et al. [13] proposed a QZS isolator using a pair of mutually repelling permanent magnets in parallel with a pneumatic spring and analyzed the static and dynamic behavior of different system configurations. Experiments showed a vibration amplitude reduction in resonance, but due to the low damping, significant resonance peaks were still present in the transfer function. Zheng et al. [14] proposed a QZS joint, in which a magnetic torsional spring, composed of two coaxial ring magnets, compensates for the positive stiffness contribution of an elastomeric spring. Zhou et al. [15] produced a six-degree-of-freedom QZS platform isolator implementing a negative stiffness mechanism with ring magnets. This platform was able to effectively attenuate a wide range of low-amplitude and high-damping force inputs. Dai et al. [16] propose a limb-like mechanism inspired by the lower limbs of kangaroos to isolate a satellite from impacts due to the capture mechanism; the system was composed of rods simulating bones and springs simulating muscles. They found that shorter arms resulted in greater attenuation of external forces. Sun et al. [17], inspired by the skeletal structure of bipeds, proposed an X-shaped isolator. In this study, they proposed an Origami-Joint Flexible structure capable of effectively attenuating impacts. Deng et al. [18] reproduced the typical structures of vertebrates with long necks, implementing a multi-layer architecture where each layer consists of the three-spring model. In Ref. [19], a bio-mimetic QZS isolator was compared with two "traditional" QZS isolators, demonstrating that the bio-mimetic structure achieved a lower resonance frequency, a smaller response peak, and eliminated hardening effects and jump-down.

Research in the automotive field regarding QZS isolators is limited; major studies focus on designing them as a secondary suspension, typical for heavy-duty vehicles such as trucks or buses, aiming to provide greater driver comfort [6]. Suman et al. [20] integrated

the Three-Spring model, analyzed in detail by Carrella et al. [3], into the structure of a traditional suspension for off-road applications related to a Double Wishbone Suspension scheme. Additionally, Mohit Saini [21] integrated a QZS isolator, a structure with curved beams, into a Push-Rod suspension scheme. It is also proposed as an active suspension by integrating two actuators at the ends of the curved beams capable of modifying the equivalent stiffness in real time [21].

Active isolation methodologies were proven to be effective in civil and aerospace applications [22,23] and also appear promising in automotives, even though real applications are not yet ready. Recent automotive studies have explored advanced active control strategies to enhance ride comfort and vehicle performance, including optimization-based PID (Proportional–Integral–Derivative) tuning and fuzzy logic approaches, as well as model predictive control frameworks with road preview information [24–27]. Conversely, passive dynamic absorbers find wide applicability in engineering [28–30].

In addition to these approaches, inerter-based vibration isolation devices have been extensively investigated as an effective solution for improving low-frequency vibration isolation in vehicle dynamics and mechanical systems. Comprehensive reviews have highlighted their theoretical foundations, physical realizations, and applications in vibration control [31].

The concept of QZS found interesting applications in different engineering fields; interesting theoretical and experimental investigations can be found in Refs. [32,33], where the concept of QZS was replaced by the High Static Low Dynamic Stiffness paradigm; in such works, the critical impact of friction on the overall suspension performance was stigmatized.

In Ref. [34], the concept of "Meta Structure" was experimentally investigated; this was an attempt to solve the aforementioned friction problems of mechanisms in the realization of QZS by introducing novel concepts of elastic non-linear structural elements. Vibration suppression can also be achieved by means of actions on the design parameters of mechanical systems, see, e.g., Ref. [35], regarding the phasing implications on the gear vibration generation.

In Ref. [36], an insightful study demonstrating how inclined trapezoidal beams achieve practical QZS behavior was published. Simulations and experiments confirm reduced natural frequency and strong low-frequency isolation, offering a promising passive solution for precision applications. A solid contribution demonstrating how adjustable quasi-zero stiffness and damping enable stable, broadband vibration suppression in robotic drilling can be found in Ref. [37]. The semiactive strategy effectively avoids resonance and improves precision under varying ambient disturbances.

A comprehensive, well-structured review, Ref. [38], clarifies QZS principles, categorizes passive and active realizations, and highlights future research needs, offering valuable guidance for designing next-generation low-frequency vibration isolation systems. A well-structured study demonstrating how a tunable bio-mimetic X-shaped isolator achieves quasi-zero stiffness and ultra-low-frequency control, delivering remarkable seismic vibration reduction for offshore platforms with high load-bearing reliability, can be found in Ref. [39].

Ref. [40] integrates quasi-zero stiffness design, sliding-mode control, and magnetorheological damping to achieve robust vibration suppression. Simulations demonstrate significant improvements over passive and PID methods, highlighting strong potential for precision robotic machining. This work focuses on a detailed multibody dynamics assessment of the suspension behavior under realistic road excitations, with particular attention to vibration isolation and ride comfort.

The present work addresses the design and verification of a potential application of the QZS isolators in automotive sector applications. Specifically, the aim is to apply

this type of isolator as the primary suspension of a vehicle. Implementing a primary suspension could have a broader range of applications and provide ride comfort to all vehicle occupants rather than just the driver. With the primary objective of improving ride comfort and suppressing vibrations and forces typically generated by ground contact, as well as addressing the static load–stiffness compromise, the choice of application was based on three critical aspects. Firstly, a preliminary classification of the vehicle based on road approval was considered. Secondly, the question was posed regarding whether the vehicle is heavy-duty or light-duty. This consideration aims at a general pre-configuration of the parameters in the mathematical model to be implemented, such as the suspended mass value. Finally, after considering the above classifications, the choice was based on aspects such as common suspensions, cost-effectiveness, and driving dynamics.

2. Multibody Model

The choice of the suspension model falls on the standard Double Wishbone Suspension system from the suspension system example present in the Adams tutorial kit for mechanical engineering courses [41,42]. The decision considered technical aspects and followed the approach of the article by Suman et al. [20], chosen as a reference. A functional schematic of the suspension in its final version is shown in Figure 1. Modifications were subsequently applied to the MSC Adams® model to obtain two comparable models of the Quarter Car Model with traditional suspension and non-linear QZS suspension. The standard structure, whose geometry has not been modified, consists of nine main components—Ground, Lower Arm, Upper Arm, Spindle Wheel, Tie Rod, Steering Rack, Body Ground, Chassis, Strut Lower, and Strut Upper—as illustrated in Figure 2.

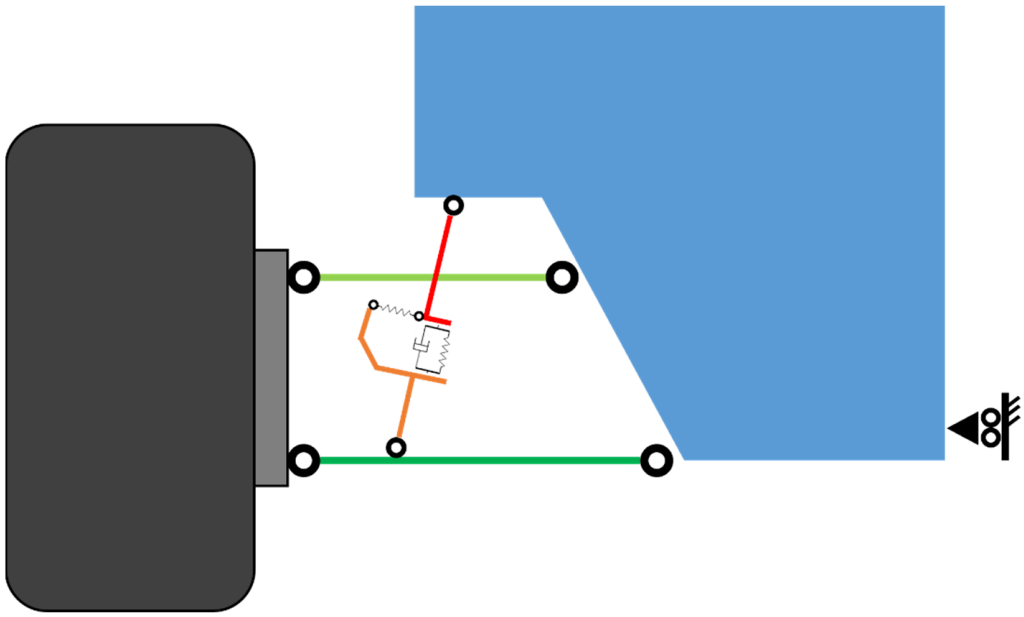

Figure 1. Functional diagram of Double Wishbone Suspension with QZS mechanism.

The ground body is the main reference system in the multibody environment, where it represents the ground or the main system of axes in the 3D model space. It is assigned a set of points that determine the main spatial points of the suspension geometry, specifically the connection points between the different elements of the mechanism: points from HP1 to HP6 determine the geometry of the two swing arms, Upper and Lower Arm, which are constrained to the Ground through two Revolute Joints that allow rotation around the local *z*-axis. The ends of the swing arms (HP3, HP6) are connected to the Spindle Wheel through two Spherical Joints that allow three rotations (Figure 3). The Tie Rod is connected to the

Spindle Wheel via a Spherical Joint (Figure 4). Finally, the Tie Rod is constrained to the Steering Rack by a Hooke-type joint that constrains the rotation between the two bodies around their principal axes, and the translations, leaving angular misalignment around the remaining axes free. The Steering Rack is fixed to the Body Ground, and the Body Ground is fixed to the Ground. The two remaining bodies, Strut Upper and Strut Lower, are constrained to each other through a Translational Joint, allowing only sliding along the common axis, and relatively constrained to Ground through another Hooke-type joint (Figure 5) and Lower Arm with a Spherical Joint (Figure 6). A summary of all components and their corresponding connection points is provided in Table 1.

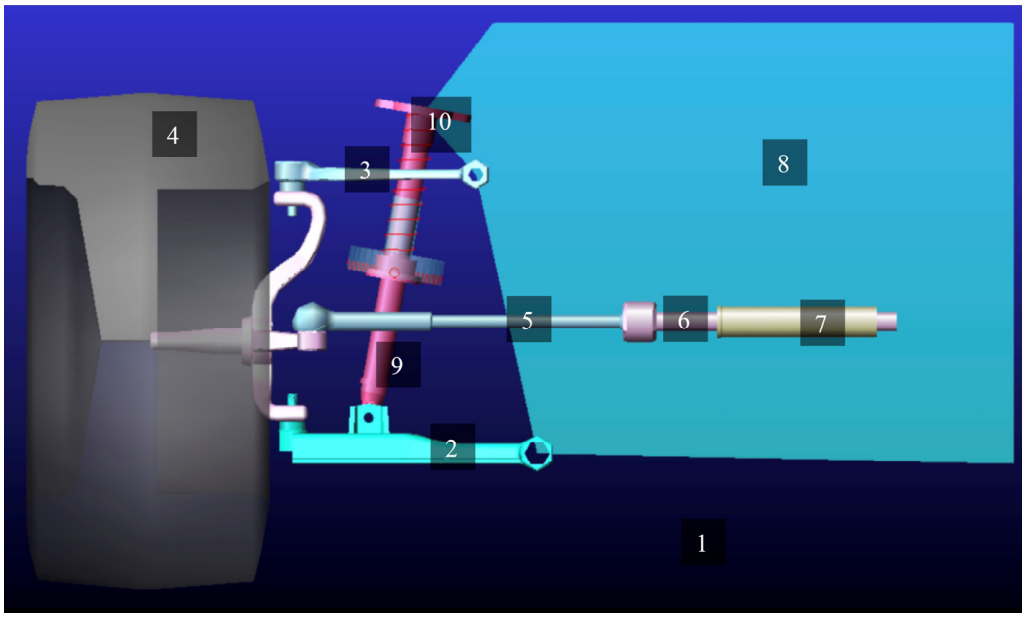

Figure 2. The main components are (1) Ground, (2) Lower Arm, (3) Upper Arm, (4) Spindle Wheel, (5) Tie Rod, (6) Steering Rack, (7) Body Ground, (8) Chassis, (9) Strut Lower, and (10) Strut Upper.

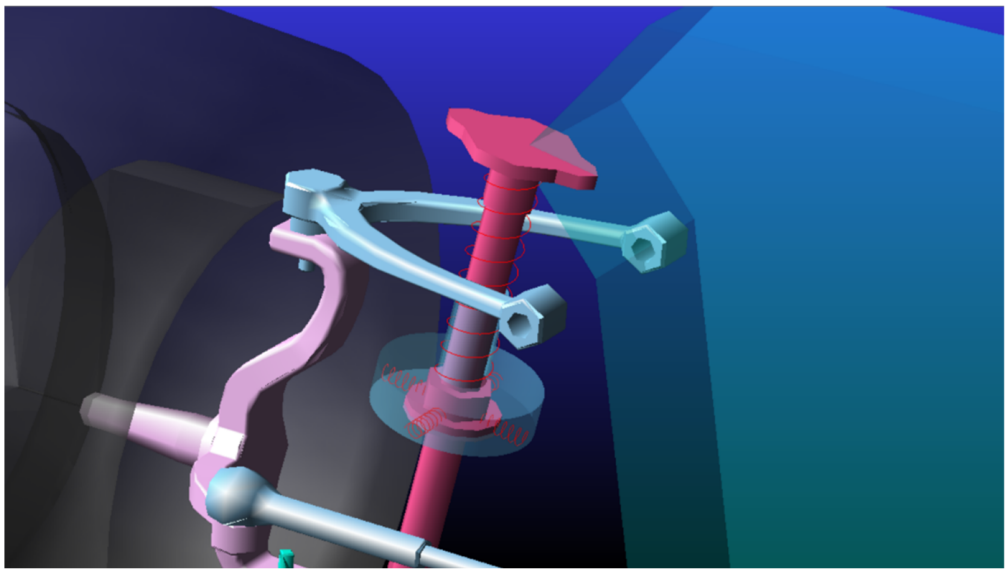

Figure 3. Spherical Joint of Upper Arm with Spindle Wheel—HP4.

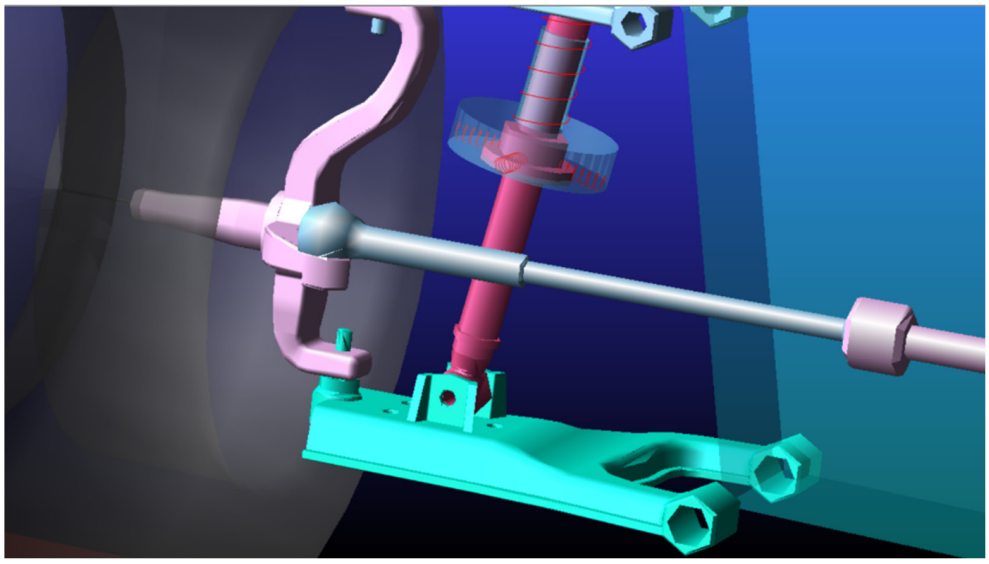

Figure 4. Spherical Joint of Tie Rod with Spindle Wheel—HP5.

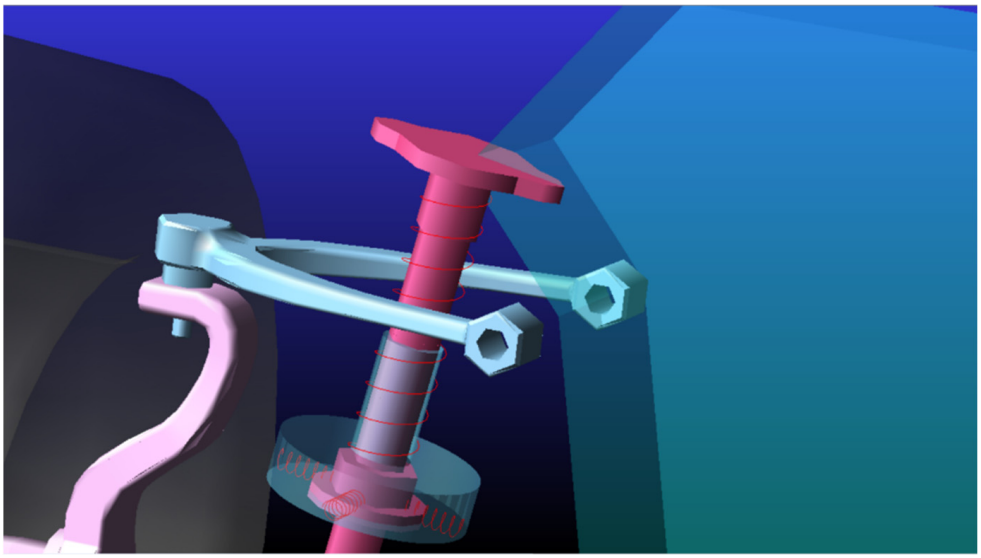

Figure 5. Hooke Joint of Strut Upper with Ground.

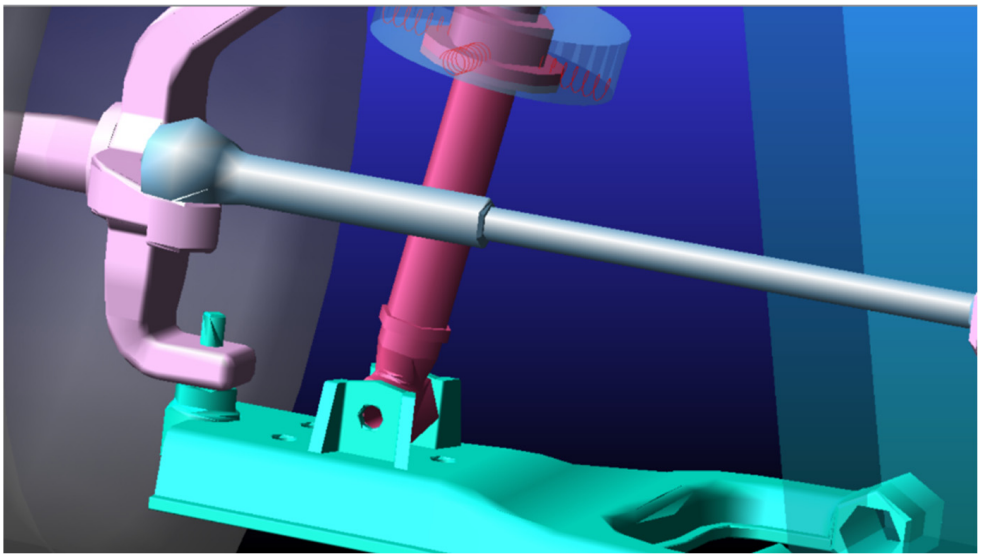

Figure 6. Spherical Joint of Strut Lower with Lower Arm.

Table 1. Components and connection points of the suspension mechanism.

No.	Component/Joint	Type of Joint	Description/Function
1	Ground	-	Global reference body: defines the fixed coordinate system of the model.
2	Lower Arm	-	Links the Chassis to the Spindle; defines the lower control geometry of the suspension.
3	Upper Arm	-	Provides upper linkage; maintains wheel camber and roll center geometry.
4	Spindle (Wheel Hub)	-	Connects the Upper and the Lower Arms to the wheel assembly and transmits forces.
5	Tie Rod	-	Transfers steering input from the Steering Rack to the Spindle.
6	Steering Rack	-	Converts rotational steering input into linear displacement of the Tie Rods.
7	Body Ground	-	An intermediate fixed body linking the Steering Rack and Chassis, attached to the Ground.
8	Strut Lower	-	Lower attachment point of the spring–damper assembly, connected to the Lower Arm.
9	Strut Upper	-	Upper attachment point of the spring–damper assembly, connected to the Chassis.
10	Chassis	-	Represents the suspended mass of the vehicle; connected to the suspension via strut and arms, and to the Ground through a vertical Translational Joint (y-axis).
11	HP1	Revolute Joint	Connection between Lower Arm and Ground (Chassis-side).
12	HP2	Revolute Joint	Connection between Upper Arm and Ground (Chassis-side).
13	HP3	Spherical Joint	Connection point defining the Lower Arm–Spindle geometry (spherical joint).
14	HP4	Spherical Joint	Connection between Upper Arm and Spindle.
15	HP5	Spherical Joint	Connection between Tie Rod and Spindle.
16	HP6	Hooke Joint	Connection point defining the Tie Rod–Steering Rack constraint (Hooke joint).

This model was slightly modified to obtain a final version of the traditional Double Wishbone Suspension: firstly, an additional body representing the vehicle frame was added. This body, appropriately named Chassis, is positioned between the suspension and the Ground. It replaces the direct constraints to the Ground or Body Ground of the Strut Upper, Upper Arm, Lower Arm, and Steering Rack with connections to the Chassis. The Chassis itself is constrained to the Ground through a Translational Joint along the vertical y-axis. In doing so, the model changes from a single-degree-of-freedom mechanism to a two-degree-of-freedom mechanism, involving the vertical motion of the suspended mass (Chassis) and the vertical motion of the vehicle wheel assembly. Subsequently, a force element was added, characterized by stiffness K_v and damping C_v, between Strut Upper and Strut Lower to model the viscoelastic force of the suspension. In particular, P_v and P_h represent the static preload forces of the vertical and horizontal springs, respectively, while K_{cv} denotes the equivalent stiffness contribution associated with the vertical spring configuration.

Once the traditional suspension model with two degrees of freedom for attenuation and isolation performance comparison was obtained, it was further modified to replicate the QZS suspension structure as a reference [20].

Compared to the baseline suspension layout shown in Figures 1–6, the QZS configuration in Figures 7 and 8 is obtained by replacing the linear spring–damper branch with an oblique-spring mechanism. Specifically, four inclined springs are introduced between the Strut Upper and Strut Lower bodies. To accommodate their lower endpoints, the Strut Lower geometry is modified by expanding it to a radius of 60 mm, and four attachment points are defined at 90° intervals at a radial distance a from the central point (354). The upper ends of the springs are fixed to the Strut Upper at a point located a distance h from point 354, where h represents the spring height under static conditions. These modifications constitute the essential changes enabling the quasi-zero-stiffness behavior and are not present in the baseline suspension model. To complete the suspension modeling, additional variables useful for parameterizing the mechanism were defined: alpha, K_v, P_v, P_h, KC_v. Alpha corresponds to the ratio between the stiffness of the vertical spring K_v and the individual horizontal spring K_h. P_v and P_h are the respective preloads due to the static deflection of the suspension. C_v corresponds to the damping coefficient of the suspension.

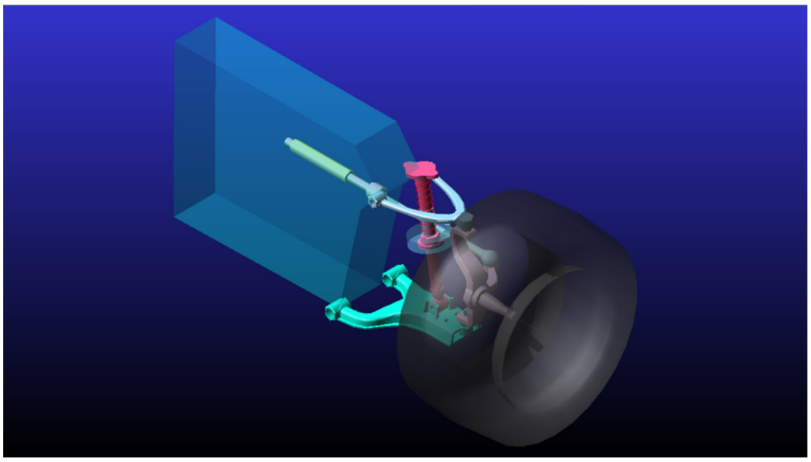

Figure 7. Traditional suspension model with 2 DOF Chassis. The baseline layout is shown in Figures 1–6, whereas the QZS-related modifications are detailed in Figure 8.

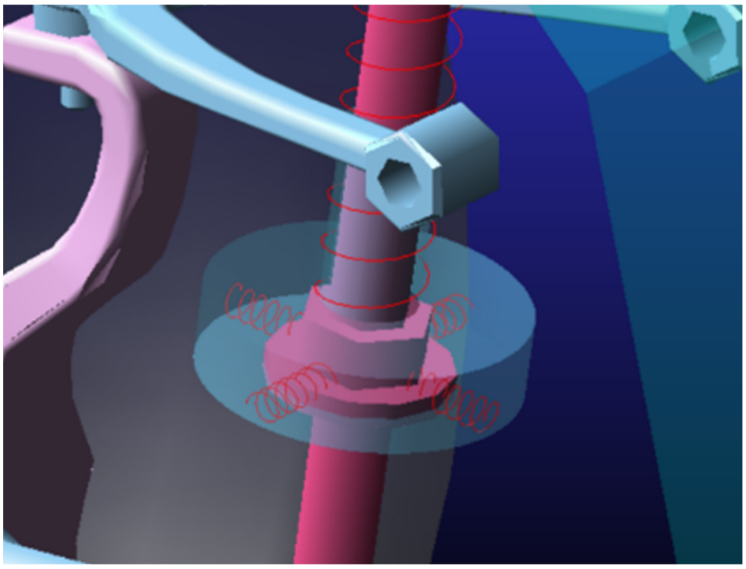

Figure 8. Details of oblique springs. The inclined springs and added attachment points represent the modifications introduced with respect to the baseline model (Figures 1–6).

3. QZS Structural Simulation

3.1. Theoretical Dimensioning

Once the multibody model was completed, the characterization of the parameters involved in the Quarter Car Model was addressed. This design step was based on the approach of Carrella et al. [3] using the model shown in Figure 9. Considering that the geometry of the reference multibody model remains unchanged, the proposed modification only involves the replacement of the linear spring–damper system with the non-linear QZS structure. As per the treatment, the force relationship was expressed in dimensionless form by normalizing the force F with respect to the reference stiffness K_0 (N/m), and the reference length L_0(m) was first determined. This force, with the contribution of only the oblique springs, is defined in Equation (2a).

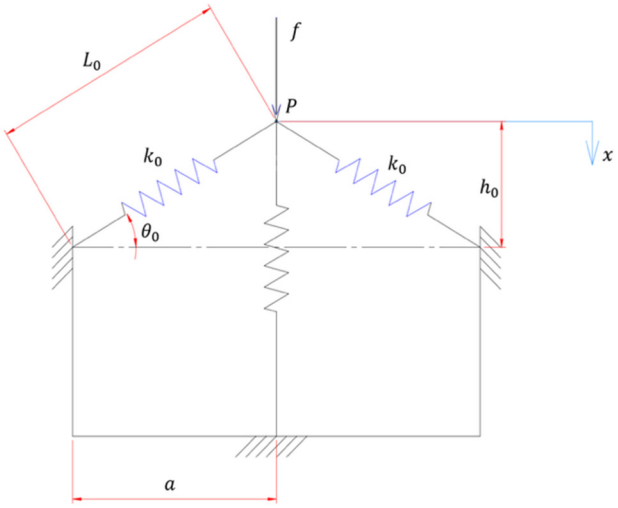

Figure 9. Model with oblique springs considered for sizing.

K_h denotes the stiffness of the oblique horizontal springs. The term K_0 is used only as a reference stiffness for the non-dimensional formulation, L_0 is the rest length, and L is the length once compressed, and θ is the initial angle described by the springs. This relationship can be transformed into dimensionless form with respect to K_0L_0 by considering the following relationships. Following the dimensionless formulation proposed in the vehicle dynamics literature [43], the force–displacement relationship is expressed as

$$f = 4K_0(L - L_0)\sin\theta \tag{2a}$$

$$\begin{cases} \sin\theta = \frac{(h_0 - x)}{L} \\ L_0 = \sqrt{{h_0}^2 + a^2} \\ L = \sqrt{(h_0 - x)^2 + a^2} \end{cases} \tag{2b}$$

By combining Equation (2a,b), one obtains

$$\frac{f}{K_0L_0} = 4(\sqrt{1-\gamma^2} - \hat{x})\left\{\left[\hat{x}^2 - 2\hat{x}\sqrt{1-\gamma^2} + 1\right]^{-1/2} - 1\right\}\sin\theta \tag{3}$$

where $\hat{x} = x/L_0$ is the dimensionless displacement, while $\gamma = \cos\theta = x/L_0$ is the geometric parameter. When γ is 0, we have horizontal springs, and when it is 1, we have vertical springs. Summing this contribution to the component of only the vertical

spring in dimensionless form results in the equivalent dimensionless force contribution given by Equation (4):

$$\hat{f} = \hat{x} + 4(\sqrt{1-\gamma^2} - \hat{x})\left\{\left[\hat{x}^2 - 2\hat{x}\sqrt{1-\gamma^2} + 1\right]^{-1/2} - 1\right\}\sin\theta \tag{4}$$

where $\alpha = K_v/K_0$ is the stiffness ratio.

At fixed α, Equation (4) defines a family of dimensionless force–displacement characteristics parameterized by the geometric ratio γ. As γ increases, the slope of the curve in the vicinity of the equilibrium position progressively decreases; values close to the quasi-zero stiffness condition lead to an almost flat response around equilibrium, whereas larger γ values may introduce a local negative slope, i.e., a negative-stiffness region. These trends are consistent with the behavior reported in Carrella et al. [3].

Differentiating with respect to displacement yields the equivalent dimensionless stiffness, one obtains the tangent stiffness $\hat{K} = \hat{K}(\hat{x})$:

$$\hat{K} = 1 + 4\alpha\left[1 - \frac{\gamma^2}{\left(\hat{x}^2 - 2\hat{x}\sqrt{1-\gamma^2} + 1\right)^{3/2}}\right] \tag{5}$$

The dimensionless equivalent stiffness $\hat{K}(\hat{x})$, defined by Equation (5), depends on the geometric parameters α and γ. The parameter α represents the ratio between the vertical and oblique spring stiffnesses, while γ is a geometric ratio related to the spring inclination. In the following analysis, α = 0.3 is adopted, and the influence of γ on $\hat{K}(\hat{x})$ can be directly inferred from Equation (5) and is consistent with the trends reported in Carrella et al. [3]. In particular, as γ approaches γ_{QZS}, the tangent stiffness around the equilibrium decreases toward zero, whereas values above γ_{QZS} may lead to locally negative stiffness near the equilibrium region.

According to Equation (4) and as reported in Carrella et al. [3], a negative slope of the force–displacement characteristic corresponds to a region of negative stiffness, indicating an intrinsically unstable configuration. The parameter γ_{QZS}, obtained from Equation (6), defines the condition of quasi-zero stiffness at the equilibrium point. In the present analysis, the value of α was kept constant (α = 0.3), leading to $\gamma_{QZS} \approx 0.55$.

These force and stiffness relationships show that the static equilibrium position, defined by $f(\hat{x}_e) = 0$, occurs at $\hat{x}_e = \sqrt{1-\gamma^2}$. The condition of zero stiffness, instead, corresponds to the point where the slope of the force–displacement curve becomes zero ($\mathrm{d}f/\mathrm{d}\hat{x} = 0$). The parameter γ_{QZS} is therefore chosen so that both conditions approximately coincide, providing a quasi-zero stiffness behavior around the equilibrium position. This value is obtained by evaluating the stiffness at the static equilibrium point, defined by the condition $f(\hat{x}_e) = 0$, and the restoring forces from the vertical and oblique springs are balanced, resulting in zero net force on the mass. This equilibrium refers to the static configuration of the mechanism, not to the zero-stiffness condition, which depends on the slope of the force–displacement curve.

$$\gamma_{QZS} = \frac{4\alpha}{4\alpha + 1} \tag{6}$$

This equation illustrates how γ influences the stability of the system. When γ is equal to $\gamma_{QZS} \approx 0.545$, a quasi-zero stiffness region appears around the equilibrium point. For values of γ lower than γ_{QZS}, the stiffness remains positive throughout the entire range, while for higher values of γ, the stiffness profile becomes negative near the equilibrium point, potentially leading to local instabilities.

Furthermore, by inverting Equation (6), the relationship between α and γ can be expressed as

$$\alpha_{\mathrm{QZS}} = \frac{\gamma}{4(1-\gamma)} \tag{7}$$

These latter relationships describe the configurations of the system that yield the ideal QZS characteristic (Figure 10).

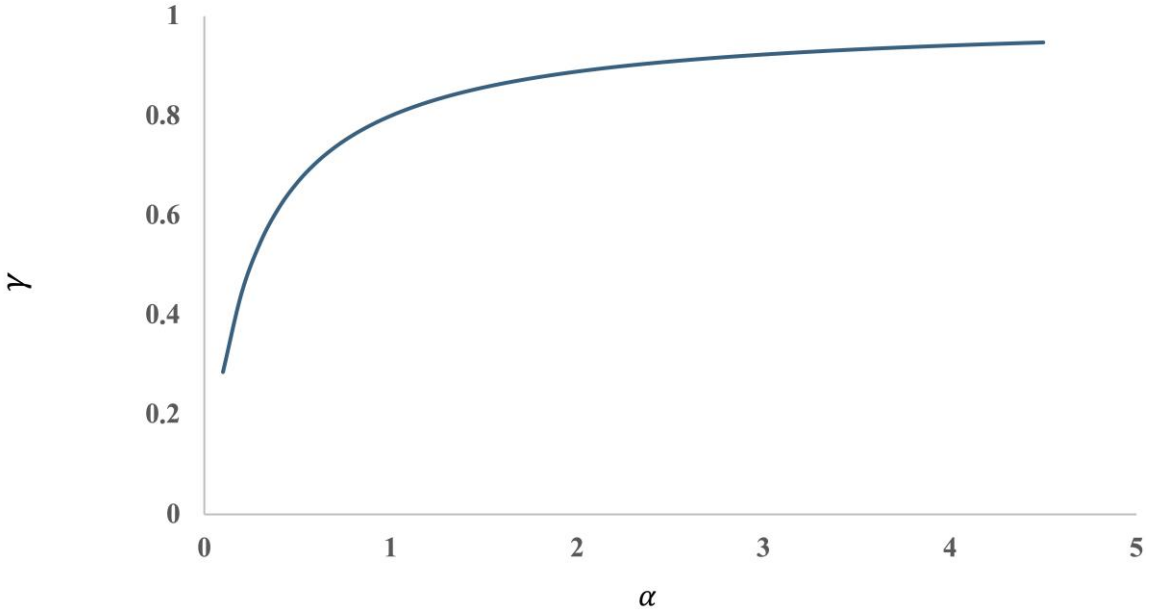

Figure 10. Relationship between γ and α.

Since there are infinite possible combinations, it is useful to define one that can improve isolation performance. For this, Carrella et al. [3] suggest an "optimal" configuration that aims to maximize the suspension travel, where the equivalent stiffness is less than a predetermined stiffness value $\hat{K}_0$, which is assumed to be equal to 1, i.e., equal to the vertical stiffness K_v. This assumption $\hat{R}_0 = 1$, corresponding to the vertical stiffness K_v, is a simplifying but strong constraint. It implies that the vertical spring dominates the overall stiffness of the system and that the oblique springs mainly contribute to the non-linear modulation around the equilibrium position. In practice, this assumption may not hold if the oblique spring stiffness is comparable to K_v, in which case the effective stiffness would deviate from unity. Nevertheless, setting $\hat{R}_0 = 1$ allows a convenient normalization and facilitates comparison between different configurations. In this optimization, $\hat{K}_{\mathrm{QZS}}(\gamma_{\mathrm{QZS}})|_{\alpha=\alpha_{\mathrm{QZS}}} = \hat{K}_0$ is evaluated, and it is solved in terms of $\hat{x}$, resulting in $\hat{x}|_{\hat{K}=\hat{K}_0} = \hat{X}_e \pm \hat{d}$, where $\hat{d}$ is the travel around the equilibrium point, normalized with respect to L_0, and is given by

$$\hat{d} = \gamma_{\mathrm{QZS}} \sqrt{\left[\frac{1}{1-\hat{K}_0(1-\gamma_{\mathrm{QZS}})}\right]^{2/3} - 1} \tag{8}$$

A relationship is obtained between the admissible travel $\hat{d}$ and the target stiffness threshold $\hat{K}_0$ by solving Equation (8). In particular, for the commonly adopted normalization $\hat{K}_0 = 1$ (i.e., stiffness normalized by K_v), the maximization yields $\gamma_{\mathrm{opt}} \approx 0.54$, which corresponds to $\alpha \approx 0.3$, in agreement with the optimal configuration reported by Carrella et al. [3].

Thus, the optimal configuration of the Quarter Car Model with Quasi-Zero Stiffness has been obtained. Evaluating $\hat{d}$ for $\hat{K}_0 = 1$, the optimum is found to be $\gamma_{\mathrm{opt}} = (2/3)^{3/2} \simeq 0.54$, which results in a value of $\alpha = \gamma_{\mathrm{opt}}/4(1-\gamma_{\mathrm{opt}}) \simeq 0.3$.

3.2. Static Dimensioning

It is necessary to clarify an aspect regarding the actual choice of the configuration: the parameters obtained from optimization are ideal and provide a configuration that could be unstable since the equivalent stiffness of the system cancels out. For this reason, and also for feasibility, approximated values of α and γ could be chosen based on a very simple criterion: remain as close as possible to the ideal condition while maintaining a positive value of the equivalent stiffness, corresponding to the region above the curve in the $\gamma - \alpha$ graph (Figure 10). The region below the curve would theoretically lead to an equivalent system with negative stiffness around the equilibrium point. For explanatory purposes, the analysis was carried out using a model scaled according to the theoretical non-dimensional parameters (α and γ) derived from the analytical formulation. A value of $a = 60$ mm has been assumed for spatial reasons, and the possible static deflection has been set as $h_0 = 92.5$ mm. With these parameters, it was possible to statically scale the mechanism by considering the equality between the dimensionless force determined by static deflection and the dimensionless gravitational load. Based on the classical Quarter Car Model formulation presented in mechanical vibration theory [1], the static scaling condition can be written as

$$\frac{K_{\text{pyld}} mg}{K_v L_0} = \hat{f} = \hat{x} + 4\alpha\left(\sqrt{1-\gamma^2} - \hat{x}\right)\left\{\left[\hat{x}^2 - 2\hat{x}\sqrt{1-\gamma^2} + 1\right]^{-1/2} - 1\right\} \tag{9}$$

From Equation (9), the vertical stiffness K_v was obtained. The corresponding horizontal stiffness K_h was then calculated using the stiffness ratio $\alpha = K_v/K_h$. These stiffness values determine the preloads applied to the multibody model, which are consistent with the static deflection of the suspension. The results of this scaling are summarized in Table 2.

Table 2. Theoretical QZS structural dimensioning parameters.

Parameter	Value	Unit	Type
α	0.298		CV
γ_{QZS}	0.544		DV
L_0	110.227	mm	CV
a	60	mm	DV
h_0	92.5	mm	CV
$\hat{x}$	92.5	mm	DV
m	100	kg	DV
$f_{\text{adim}}(\hat{X})$	0.839		CV
K_v	14.24	N/mm	CV
K_h	4.3	N/mm	CV
P_v	1317.6	N	CV
P_h	213.7	N	CV

The selection of the model parameters was based on a combined analytical and literature-based approach, rather than on numerical optimization. The stiffness parameters of the QZS suspension were derived from the theoretical quasi-zero stiffness formulation by first selecting the dimensionless parameters α and γ to achieve the desired quasi-zero stiffness condition. The corresponding physical stiffness values were then obtained by enforcing static equilibrium under the gravitational load of the quarter car mass, as described in Equation (9). The suspended mass value was chosen to represent a realistic quarter car configuration and is consistent with commonly adopted values in the vehicle dynamics literature. The damping coefficient was initially estimated using classical quarter car vibration theory and subsequently refined through parametric analyses in MSC Adams® to evaluate the trade-off between ride comfort and road holding performance. The final

parameter values adopted in the simulations therefore reflect a physically consistent and analytically grounded configuration.

The parameters listed in Table 2 describe the theoretical configuration of the QZS mechanism and its associated stiffness characteristics. The ratio between the vertical and horizontal stiffness components is represented by α, whereas γ_{QZS} is the non-dimensional parameter defining the quasi-zero stiffness condition. The geometric attributes of the system are characterized by L_0, the half-length of the unloaded curved beam, and a, which denotes the radial distance of the oblique spring endpoints from the central reference point. The static configuration is defined through h_0, the vertical static deflection, and the corresponding dimensionless displacement variable $\hat{x}$. The equivalent suspended mass of the system is indicated by m. The dimensionless force associated with the static equilibrium position, $f_{\text{adim}}(\hat{x})$, is evaluated through the non-dimensional formulation of the mechanism. The parameters K_v and K_h represent the vertical and horizontal stiffnesses of the suspension, respectively, while P_v and P_h denote the preload values acting in the vertical and horizontal directions. Together, these quantities provide the complete set of geometric, mechanical, and non-dimensional variables necessary to define and scale the QZS structural model.

A multiplicative coefficient K_{pyld} is considered in the scaling for the balance of moments acting on the two-dimensional structure of the suspension, as shown in Figure 11 and Table 3. Thus, a theoretically effective configuration of this suspension with a non-linear QZS characteristic has been obtained. The dimensionless force versus the dimensionless displacement for the theoretical configuration and the reference configuration reported in [20] is shown in Figure 12.

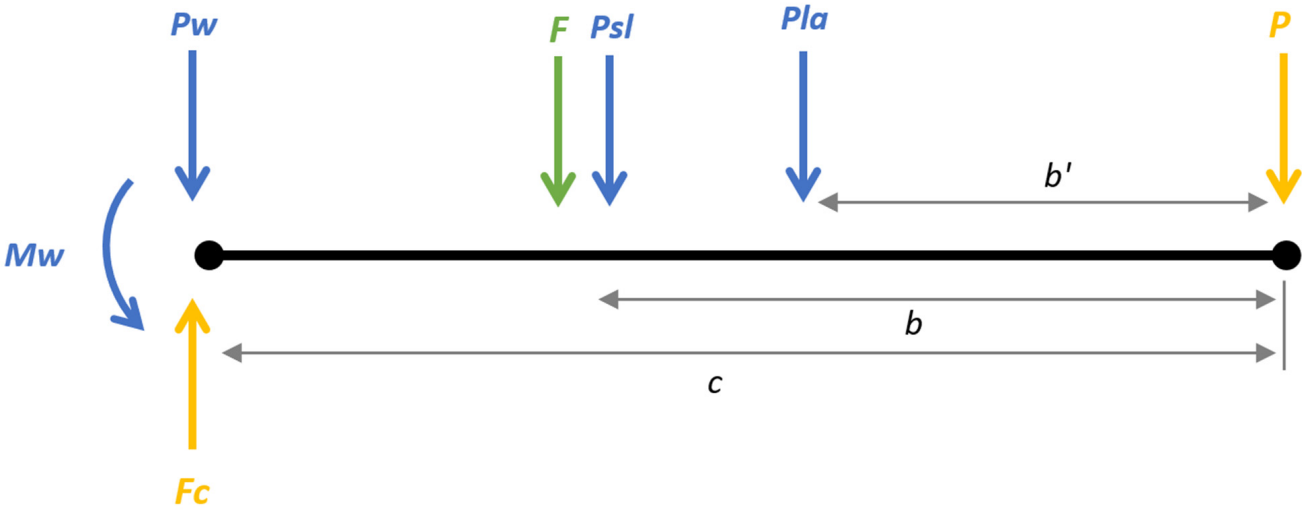

Figure 11. Static balance of the Lower Arm.

Table 3. Values of static balance scaling for the Lower Arm.

Parameter	Value	Unit	Description
P_w	29.43	N	Load applied at the wheel joint.
P_{sl}	29.43	N	Load acting on the steering link.
P_{la}	39.24	N	Load acting on the Lower Arm connection point.
M_w	1765.8	N·mm	Moment generated about the wheel axis.

Table 3. *Cont.*

Parameter	Value	Unit	Description
F_c	981	mm	Distance between the central joint and spring connection point.
c	305	mm	Horizontal distance between suspension arm joints.
b	210	mm	Vertical distance between the Lower Arm pivots.
$b\prime$	145	mm	Offset distance between arm joints and spring attachment.
F	1317.1	N	Resultant static load acting on the suspension arm.
K_{pyld}	1.34		Multiplicative scaling coefficient for static balance.

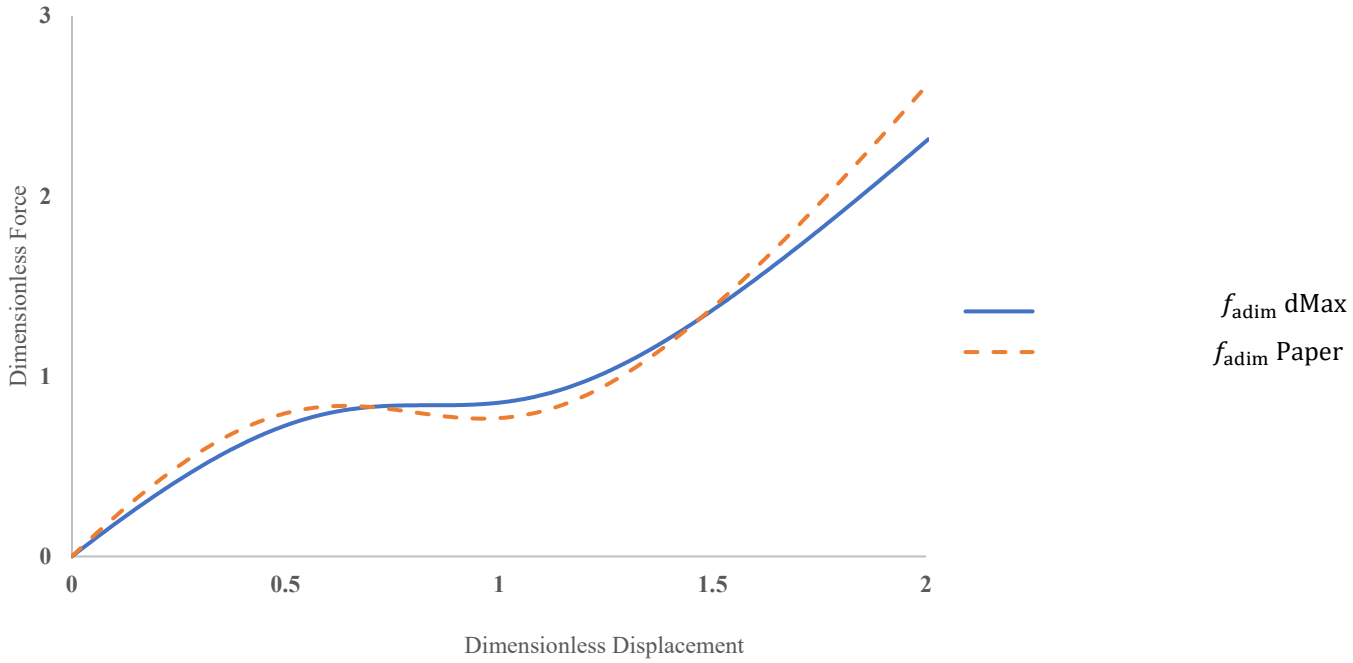

Figure 12. Comparison of the dimensionless force–displacement characteristics of the theoretical QZS configuration (solid line) and the reference configuration reported in [20] (dashed line).

Figure 11 shows the static force and moment balance acting on the Lower Arm, which is introduced to ensure mechanical consistency between the theoretical suspension dimensioning and the multibody implementation in MSC Adams®. The resulting static equilibrium configuration defines the reference position of the suspension and the preload conditions of the elastic elements. The dynamic response of the system is subsequently evaluated by analyzing the equations of motion of the Quarter Car Model around this equilibrium configuration.

The parameters listed in Table 3 define the static equilibrium condition of the Lower Arm within the QZS suspension configuration. These values are derived from the force and moment balance equations applied to the suspension geometry, considering the loads transmitted through the wheel joint, steering link, and Lower Arm connection. The moment M_w represents the torque generated about the wheel axis due to these loads. Geometric distances such as F_c, c, b, and b' are used to establish the spatial relationships between joints and spring attachment points. The resultant static force F acting on the suspension

arm is calculated based on these parameters. The coefficient K_{pyld} serves as a corrective scaling factor to reconcile discrepancies between the theoretical static balance and the multibody simulation model, ensuring consistency in both force distribution and geometric configuration (refer to Figure 11).

The slight discrepancy observed between the theoretical and reference curves in Figure 12 can be attributed to differences in the formulation of the equivalent stiffness. In the present model, the non-linear stiffness relationship was derived by explicitly considering the geometric configuration and static equilibrium conditions of the QZS mechanism, while in reference [20], a simplified analytical formulation was adopted. Despite these differences, both formulations exhibit the same overall quasi-zero stiffness behavior around the equilibrium position.

3.3. Traditional Model Dimensioning

The scaling of the Traditional model was based on the theory of vertical dynamics of the vehicle [43], which addresses the analysis of the Quarter Car Model depicted in Figure 13. This model, having 2 degrees of freedom and lumped parameters, consists of a mass, called "unsprung", representing the mass of the wheel interposed between the Ground and the suspended mass, are connected through a stiffness p, representing the tire, and a stiffness k and damping c, representing the suspension. This 2-degree-of-freedom model is governed by two dynamic equations:

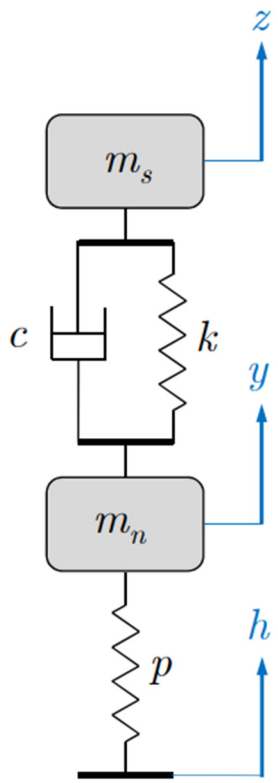

Figure 13. Quarter Car Model or single-suspension model.

The following equations governing the Quarter Car Model dynamics are derived from the standard vibration theory [44].

$$\begin{cases} m_s\ddot{z} + c(\dot{z} - \dot{y}) + k(z - y) = 0 \\ m_n\ddot{y} + c(\dot{y} - \dot{z}) + k(y - z) + p(y - h) = 0 \end{cases} \tag{10}$$

System (10) can be summarized in matrix form as

$$M\ddot{\mathbf{x}} + C\dot{\mathbf{x}} + K\mathbf{x} = h \tag{11}$$

where

$$\begin{cases} \mathbf{x} = (z(t), y(t))^{\mathrm{T}} \\ \mathbf{F} = (0, ph(t))^{\mathrm{T}} \end{cases} \tag{12}$$

Assuming the model is subjected to harmonic excitation $h(t) = H\cos\Omega t$, the suspended and unsuspended masses, after the transient has expired, will respond in sinusoidal form:

$$\begin{cases} z(t) = Z\cos(\Omega t + \phi) \\ Y(t) = Y\cos(\Omega t + \psi) \end{cases} \tag{13}$$

By expressing the harmonic displacements in complex form, $z(t) = \Re[\widetilde{Z}e^{-i\Omega t}]$ and $y(t) = \Re[\widetilde{Y}e^{-i\Omega t}]$, and substituting them into the equilibrium equations, the system can be compactly rewritten as

$$\begin{cases} \alpha\widetilde{Z} - \beta\widetilde{Y} = 0 \\ -\beta\widetilde{Z} + \gamma\widetilde{Y} = pH \end{cases} \tag{14}$$

where α, β, γ are complex coefficients that depend on the stiffness, damping, and mass parameters of the system, from which it follows that the harmonic response of the suspended mass and the unsuspended mass are

$$\begin{cases} \frac{\widetilde{Z}}{H} = \frac{p\beta}{(\alpha\gamma-\beta^2)} = \frac{p(k+ic\Omega)}{f_1(\Omega^2)+ic\Omega f_2(\Omega^2)} \\ \frac{\widetilde{Y}}{H} = \frac{p\alpha}{(\alpha\gamma-\beta^2)} = \frac{p\left(k-m_s\Omega^2+ic\Omega\right)}{f_1(\Omega^2)+ic\Omega f_2(\Omega^2)} \end{cases} \tag{15}$$

where

$$\begin{cases} f_1(\Omega^2) = m_s m_n \Omega^4 - [(p+k)m_s + km_n]\Omega^2 + pk \\ f_2(\Omega^2) = p - (m_s + m_n)\Omega^2 \end{cases} \tag{16}$$

In the study of comfort in vertical dynamics [43], it is useful to consider $\Omega^2\widetilde{Z}/H$ representing the normalized acceleration amplitude to the vehicle body.

In an initial dimensioning of the equivalent damping coefficient of the Quarter Car Model, this harmonic response is analyzed as the damping coefficient c varies. For $c = 0$, the system remains a two-degree-of-freedom model; however, its undamped formulation allows for modal decomposition, yielding two distinct natural frequencies. The first corresponds predominantly to the motion of the vehicle body (low-frequency mode), while the second is mainly associated with the unsprung mass (high-frequency mode), as illustrated in Figure 14a,b. This distinction is useful to interpret the physical contribution of each mode to the overall dynamic behavior.

These are obtained as follows:

$$\Omega^2\widetilde{Z}/H|_{c=0} = p\Omega^2\sqrt{k^2/f_1^2} \tag{17}$$

Then, by nullifying f_1, the denominator of the transfer function becomes zero, causing the response amplitude to theoretically tend to infinity—this condition corresponds to the resonance of the system.

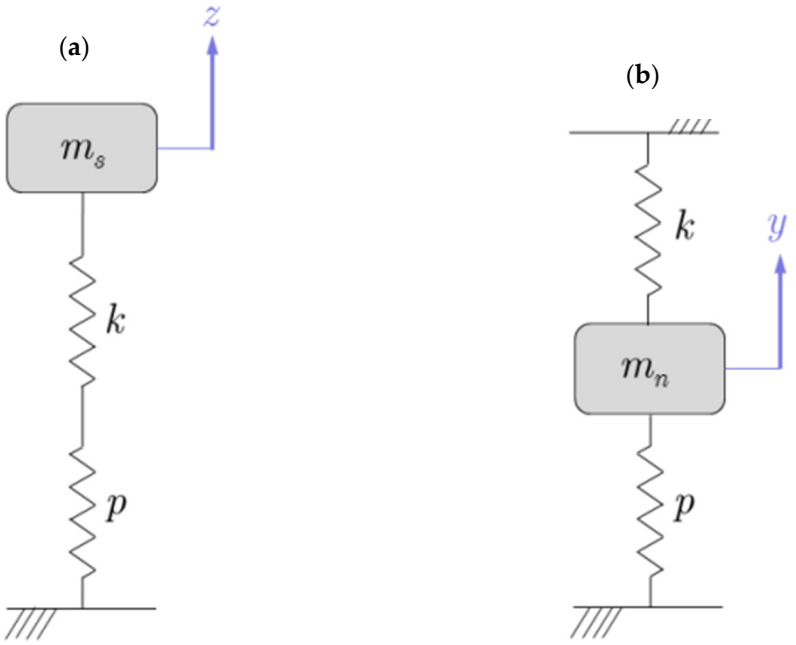

Figure 14. Equivalent mechanical systems representing the natural modes ω_1 and ω_2, corresponding, respectively, to the displacements $z(t)$, of the sprung mass, (**a**), and $y(t)$ of the unsprung mass, (**b**).

Setting $f_1 = 0$ gives $\det[\mathbf{k} - \Omega^2\mathbf{M}]$, and assuming that $m_n \ll m_s$ and $k \ll p$, it returns

$$\begin{cases} \omega_1^2 = pk/(m_s(p+k)) \\ \omega_2^2 = p + k/m_n \end{cases} \tag{18}$$

Analyzing the response for $c \to \infty$, i.e., when the intermediate spring–damper branch behaves as locked and therefore becomes dynamically ineffective, the relationship simplifies to

$$\Omega^2\widetilde{Z}/H|_{c\to\infty} = p\Omega^2\sqrt{1/f_1^2} \tag{19}$$

so that setting $f_2 = 0$ results in a single natural frequency:

$$\omega_3 = \sqrt{\frac{p}{(m_s + m_n)}} \tag{20}$$

Thus, transitioning from one extreme, $c = 0$, to the other, $c \to \infty$, the response changes from two resonance frequencies to a single one (Figure 15). However, it is noted that there are three fixed points, which prove to be independent of the damping coefficient, where the harmonic response curve always passes through.

As shown in Figure 15, the harmonic response of the Quarter Car Model exhibits three fixed points, denoted as A, B, and C, and are independent of the damping coefficient.

The compromise damping value that optimizes ride comfort is obtained by imposing a horizontal tangency condition of the harmonic response at the fixed-point A, i.e., by enforcing:

$$\frac{\delta(\Omega^2\widetilde{Z}/H)}{\delta\Omega}|_{\Omega=\Omega_A} = 0 \tag{21}$$

From which the optimal damping value for comfort is obtained:

$$c_{\text{opt}} = \sqrt{\frac{m_s k}{2}}\sqrt{\frac{p+2k}{p}}|_{p\to\infty} = \sqrt{\frac{m_s k}{2}} \tag{22}$$

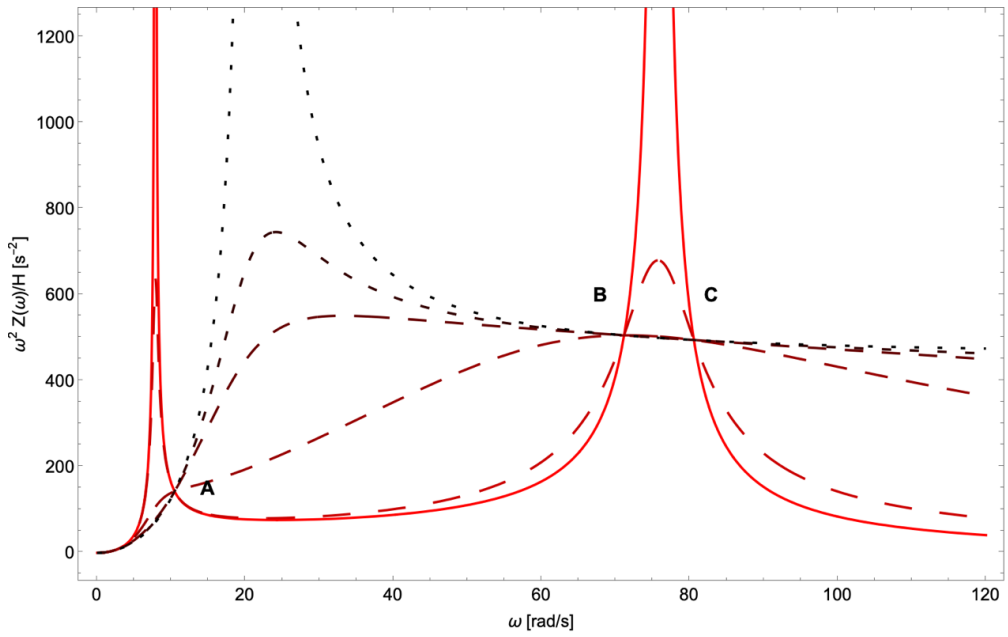

Figure 15. Normalized amplitude of the sprung mass acceleration of a Quarter Car Model with three fixed points (A, B, and C) for increasing damping values from zero to the infinite (10^{16}). The damping progression is encoded by color (zero: bright red to 10^{16}: black) and line style (zero: solid to 10^{16}: dotted).

In this derivation, the tire stiffness p is assumed to tend to infinity in order to simplify the coupled 2-DOF system into a single-degree-of-freedom equivalent model. Physically, this assumption represents a rigid tire condition, allowing the optimal damping coefficient c_{opt} to be derived analytically for the sprung mass motion.

This condition corresponds to selecting the damping value that flattens the response curve locally at the fixed-point A, thereby preventing amplification around the low-frequency resonance while maintaining acceptable isolation away from resonance.

This damping value corresponds to a damping coefficient:

$$\zeta = \frac{c_{\text{opt}}}{c_{\text{crit}}} = \frac{1}{2\sqrt{2}} \simeq 0.35 \tag{23}$$

In reality, this Quarter Car Model configuration yields suboptimal conditions for road holding, as evaluated through the harmonic response of N/pH, representing the variation in force at the Ground. To improve road holding, damping is increased to compromise values greater than the optimal comfort damping. To relate the damping acting along the suspension link to the equivalent vertical damping at the wheel hub, the transformation between the link elongation and the vertical displacement must be considered. Since the damping force depends on the velocity along the link, the equivalent damping in the vertical direction is obtained as

$$c_t = c\left(\frac{\delta L}{\delta z}\right)^2 \tag{24}$$

where $(\delta \mathrm{L}/\delta \mathrm{z})$ represents the kinematic ratio between the link elongation and the vertical motion.

From this theoretical treatment, the traditional suspension model has been dimensioned: the stiffness has been determined at the same static deflection corresponding to 92.5 mm, resulting in a value of 14.2 N/mm. Consequently, the optimal damping value, considering an average value of $\frac{\delta L}{\delta z} = 0.8$, is approximately 1312 Ns/m.

The results are summarized in Table 4.

Table 4. Values for scaling the Traditional model.

Parameter	Value	Unit
K_v	14.2	N/mm
C_v	1312	N·s/m
P_v	1313.5	N

4. Road Profile

To perform more realistic dynamic tests, random-type excitations based on ISO 8608 standards were adopted. These standards prescribe the characteristic values of Power Spectral Density based on the road profile category reflecting the pavement conditions, ranging from class A (excellent conditions) to class H (poor conditions). According to ISO 8608, the road roughness is characterized in the spatial-frequency domain by a Power Spectral Density (PSD) specification (class-dependent level and slope); therefore, the PSD definition and class parameters are taken directly from ISO 8608 and the corresponding reference source [45]. Out of numerous categories, only some were considered more interesting. Categories related to low-quality surfaces were not taken into account, as they do not reflect the most common usage conditions for a non-specialized vehicle. On the other hand, category A would not provide adverse conditions for traditional suspensions. For generating road profiles, a MATLAB code was adopted to create an array of spatial coordinate points, which were later used to define a spline in the multibody simulator MSC ADAMS. In this workflow, MATLAB® is used to generate the ISO 8608-compliant road excitation profiles and to define the corresponding spatial inputs, while MSC ADAMS® employs these profiles as spline-defined road motions for the multibody dynamic simulations. This integrated approach enables a consistent transfer of realistic road excitations from the numerical generation stage to the multibody simulation environment. This code simplifies road profile generation [46] as the superposition of N sinusoids with variable amplitude, frequency, and phase according to the law:

$$z_r(x) = \sum_{i=0}^{N} 2^k \cdot \sqrt{\Delta n} \cdot \left(\frac{n_0}{i\Delta n}\right) \cdot 10^{-3} \cdot \cos(2\pi \cdot i \cdot \Delta n \cdot x + \varphi_i) \tag{25}$$

where $\Delta n = 1/L$, with L being the total length of the road profile; $N = n_{\max}/\Delta n = L/B$, with B being the sampling interval, so $n_{\max}$ is the spatial sampling frequency; $n_0 = 0.1\ \mathrm{m}^{-1}$ is the fundamental frequency; $n_i = i\Delta n$ is the i-th frequency; φ_i is the random phase of the i-th harmonic; and k is the exponent specific to the ISO class (see Table 5). The results of this code are summarized in Figure 16, representing four ISO categories of road profiles (B, C, D, E), with which splines in MSC ADAMS were subsequently generated to define the motion.

Table 5. ISO 8608 standard values for k.

Road Class		k
Upper Limit	**Lower Limit**	
A	B	3
B	C	4
C	D	5
D	E	6
E	F	7
F	G	8
G	H	9

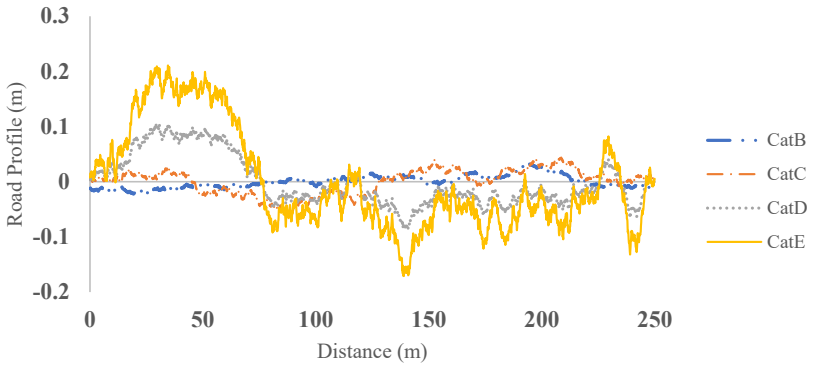

Figure 16. Road profiles class B, C, D, E.

5. Static Analysis

Analyses performed through MSC Adams on the initial models begin with static characterization, defining the force–displacement relationship characteristic of the mechanism. This aspect technically describes how the system behaves under quasi-static conditions, providing an initial understanding of its properties. To determine the force–displacement curves of the three models under analysis, a vertical translational motion was defined at the wheel hub, from one end to the other of the available stroke (±80 mm), with the Chassis fixed to the Ground. The vertical force contribution of individual springs, constituting the mechanism, was then plotted against the relative displacement in the equilibrium configuration.

From Figure 17, it can be confirmed that the theoretical characterization of the model leads to a characteristic with zero stiffness. Additionally, it is observed that this parameterization results in an equivalent stiffness curve that is lower than the vertical stiffness throughout almost the entire working range, specifically $K_{eq} < K_v$ between ±65 mm. However, it is essential to note that the analytical treatment presented here considers the suspension as a lumped linear system and therefore neglects the intrinsic geometric nonlinearity clearly visible in the force–displacement behavior of the mechanism shown in Figure 17. This nonlinearity arises from the kinematic coupling of the oblique springs and the large deflection effects, which are not captured by the simplified linear model. This approach was compared with a slightly different method: by still fixing the Chassis to the Ground and applying the same motion, the vertical force acting on the Chassis–Ground constraint was plotted.

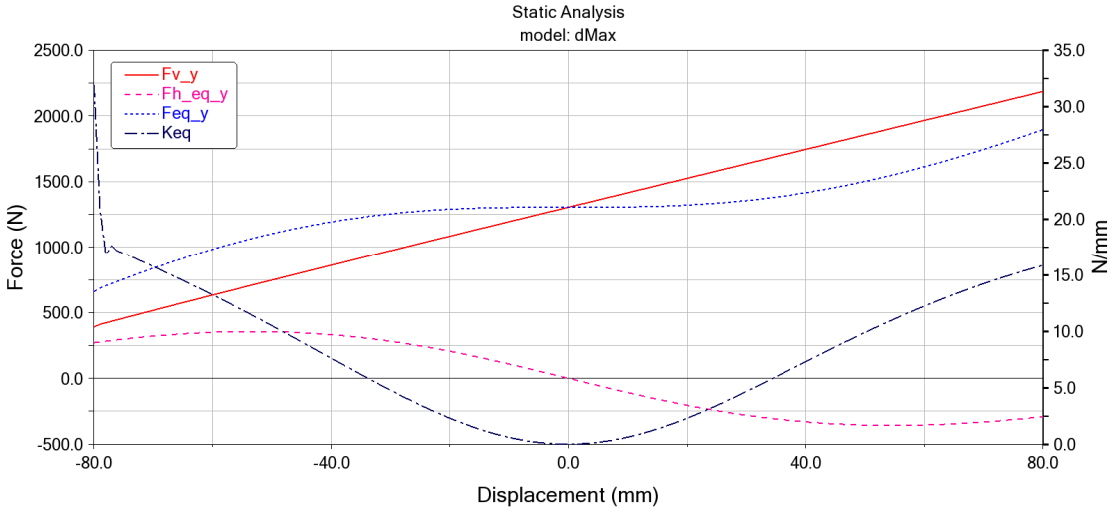

Figure 17. Static analysis of the dMax model with individual spring contributions. Results obtained from MSC Adams® simulations.

As shown in Figure 18, which represents the variation in the reaction force with respect to the vertical displacement of the Chassis (formerly indicated as "length"), the second analysis method highlighted the intrinsic nonlinearity of the suspension system, resulting in a slightly negative equivalent stiffness of -0.456 N/mm at the equilibrium point, where a zero equivalent stiffness was initially expected. This deviation from the theoretical condition can be corrected by slightly oversizing the model according to the previously described criteria, thereby shifting the parameterization toward a configuration with positive stiffness. Similarly, the reference model [20] was characterized, revealing a theoretical behavior with a negative stiffness of -4.42 N/mm at the minimum point (Figures 19 and 20).

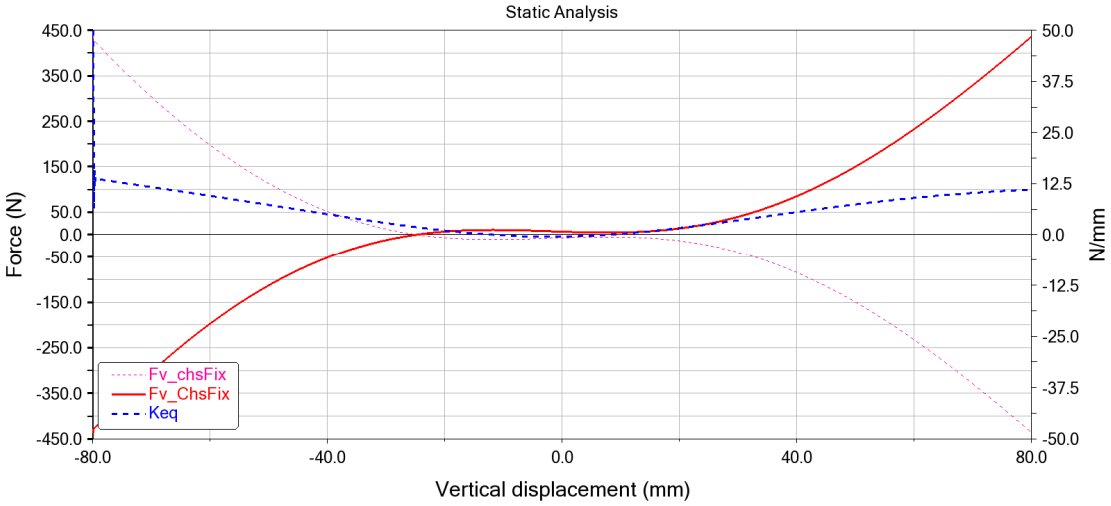

Figure 18. Static analysis of the dMax model under gravitational loading applied on the Chassis–Ground constraint. The plot shows the reaction force as a function of the vertical displacement (mm) of the Chassis relative to the ground, highlighting the non-linear stiffness behavior of the QZS suspension mechanism. Results obtained from MSC Adams® simulations.

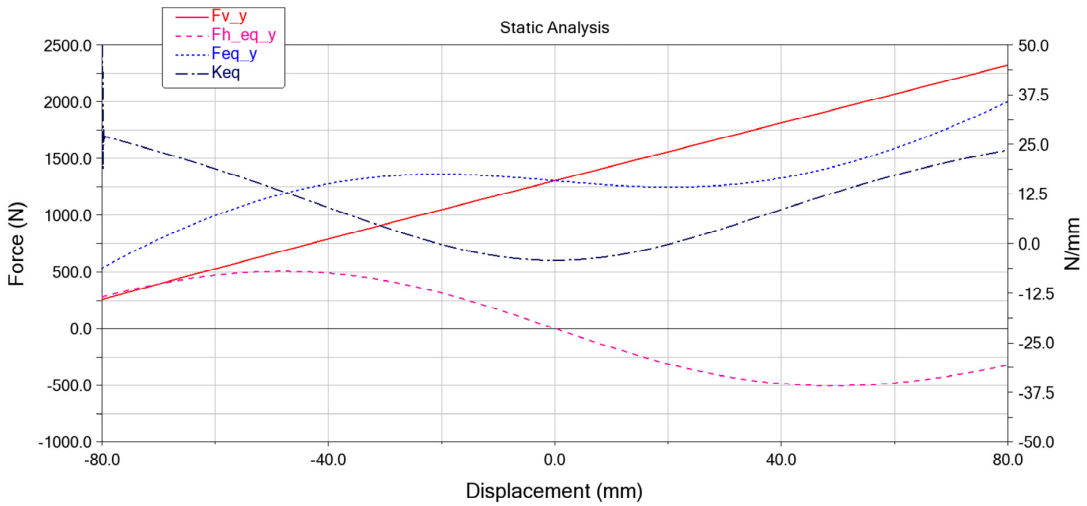

Figure 19. Static analysis of the reference model with individual spring contributions. Results obtained from MSC Adams® simulations.

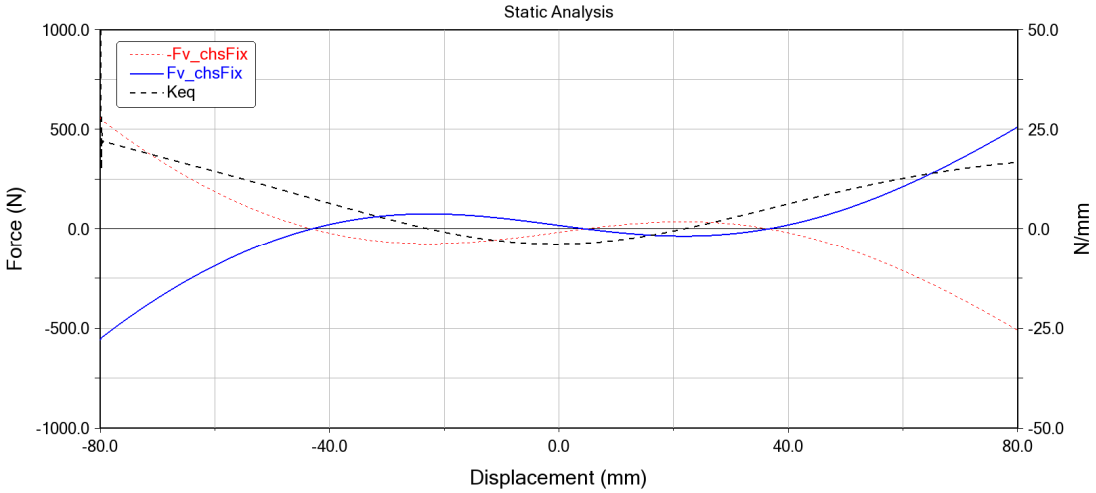

Figure 20. Static analysis of the reference model through gravitational force on the Chassis–Ground constraint. Results obtained from MSC Adams® simulations.

In any case, the nonlinearity of the suspension system minimally affected the static characteristics of the suspension, and the scaling discussed in the previous chapter was considered sufficiently reliable. Finally, the static characteristic of the traditional (linear) suspension is included in Figure 21 for reference and validation purposes. The comparison confirms that the geometric configuration of the suspension has a minimal effect on the overall static force–displacement response, which remains essentially linear.

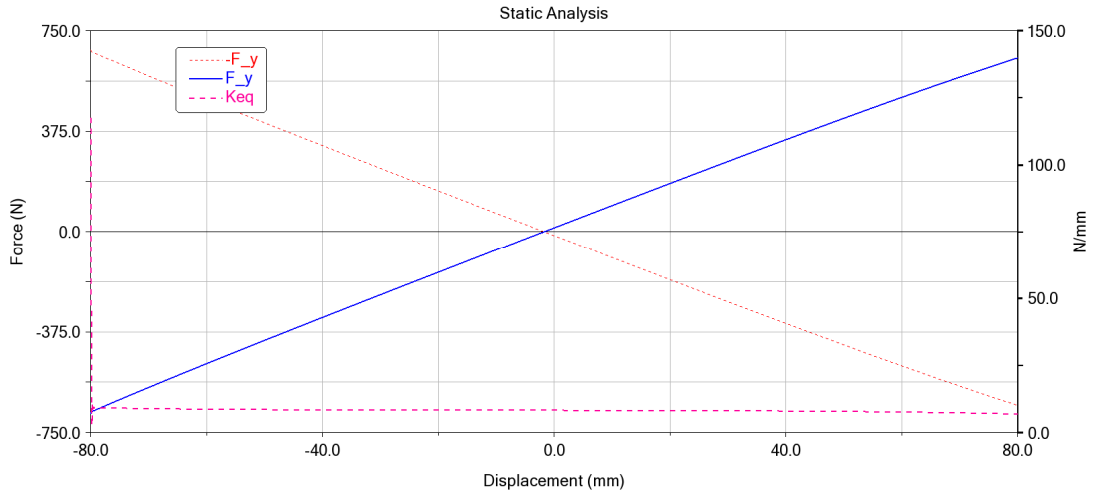

Figure 21. Static analysis of the Traditional model through gravitational force on the Chassis–Ground constraint. Results obtained from MSC Adams® simulations.

Small fluctuations observed around the −80 mm displacement in the stiffness curves are due to numerical artifacts. Since the simulation is initialized with the wheel hub already positioned at −80 mm relative to the assembly reference, minor computational errors appear during the calculation of derivatives and measured quantities at the beginning of the simulation.

6. Dynamic Analysis

For dynamic analyses, an automated methodology was developed to generate transmissibility curves characterizing the three models. Specifically, the curves of the ratios between the RMS values of the output (Chassis) and input (wheel group) were analyzed. The Chassis and wheel responses were selected as performance indexes, while they repre-

sent, respectively, the sprung-mass response related to ride comfort and the unsprung-mass response associated with road excitation; for this reason, the responses of the Traditional and dMax models are directly compared using the same Chassis and wheel signals under identical excitation conditions.

Dynamic analyses with specific forcing functions were also conducted to evaluate the attenuation of RMS acceleration values. To achieve this, a sinusoidal translational motion applied to the wheel hub, dependent on two design variables of amplitude and frequency, was first implemented in the multibody models. Utilizing the measure related to the Chassis motion, a Design Study was set up in MSC Adams to study the Chassis response with varying only the frequency of the forcing function across 50 levels. By plotting each of the 50 Chassis responses over time and evaluating the steady-state behavior (the simulation length was adjusted to the minimum frequency, ensuring an adequate number of periods), these time responses were exported in tabular form to MATLAB®. The RMS of the response, calculated after removing its mean value (i.e., zero-mean signal), was then evaluated using MATLAB®. This Design Study was repeated for each model with three different forcing amplitudes: 50, 25, and 5 mm, to assess their influence as the systems under analysis are strongly non-linear. Reference [20] and the dMax model correspond to the configuration exhibiting the maximum static deflection obtained from the parametric analysis of the QZS suspension, used here as a representative nonlinear configuration for dynamic evaluation. In the models, the transmissibility for high-amplitude forcing was determined in two "cycles" to densify the number of points to interpolate around the natural frequencies. The dMax model corresponds to the configuration exhibiting the maximum static deflection obtained from the parametric analysis of the QZS suspension, used here as a representative non-linear configuration for dynamic evaluation. The first cycle covered the range 1.5–15 Hz, and the second cycle covered only the range 0.1–1.5 Hz. This additional step aimed to represent the nonlinearity of the models' transmissibility; however, this curvature, which should appear near-resonance, is not reflected due to the lack of passing final simulation conditions as initial conditions for the subsequent one. Consequently, the point series represents only part of the complete curve. The transmissibility of the three models under optimal conditions, i.e., with low amplitude forcing, is shown in Figure 22.

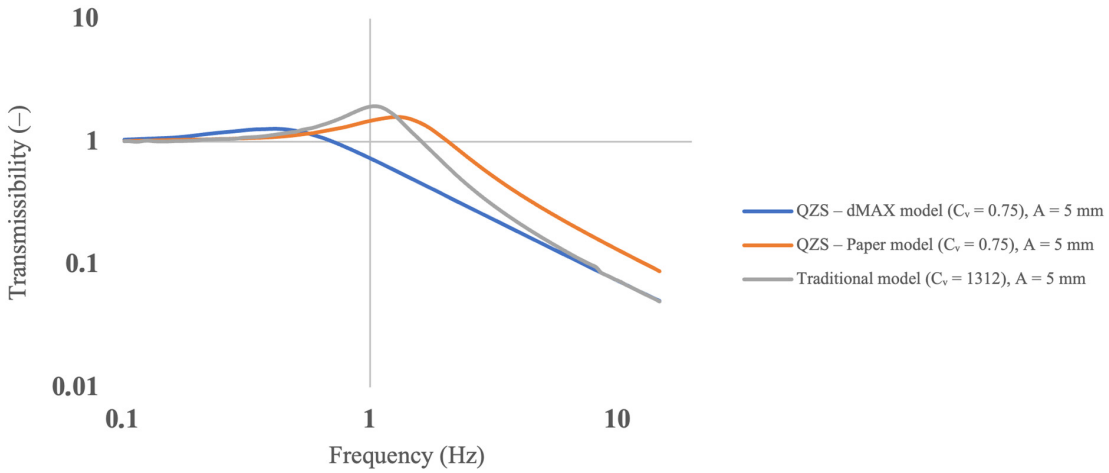

Figure 22. Transmissibility curve of the dMax, Paper, and Traditional models with a forcing amplitude of 5 mm.

The main characteristic of the QZS suspension is the lowering of the natural frequency of the system. It also allows obtaining lower transmissibility values at resonance compared to the Traditional model. The transition is from the Traditional model with a range of around 1.3 Hz to the dMax model with a resonance peak around 1 Hz, significantly

reducing transmission for higher frequency forcing. Subsequently, the discussion continues for larger amplitudes in Figures 23 and 24.

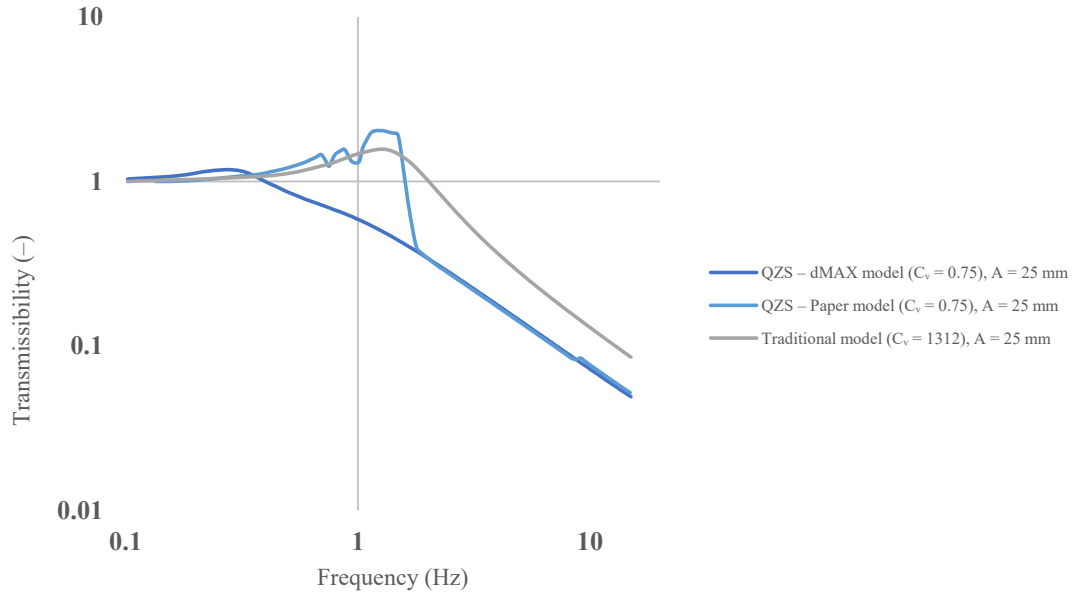

Figure 23. Transmissibility curve of the dMax, Paper, and Traditional models with a forcing amplitude of 25 mm.

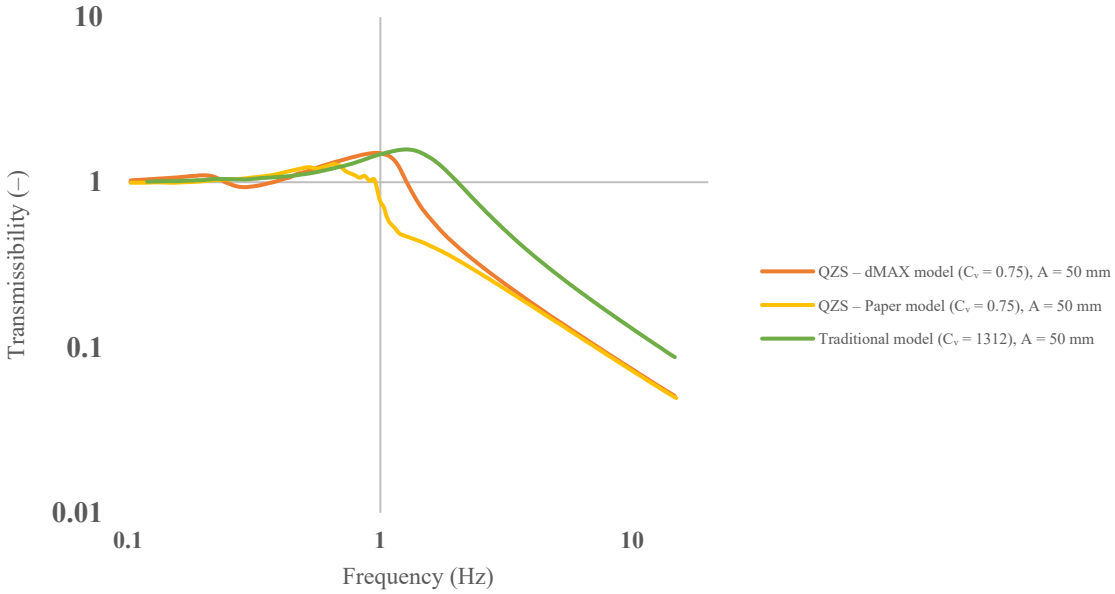

Figure 24. Transmissibility curve of the dMax, Paper, and Traditional models with a forcing amplitude of 50 mm.

Previously, the influence of damping, attributed only to the vertical component, in the harmonic response of nonlinear systems was also investigated. The QZS suspension models were originally formulated without damping; however, including a damping term is essential for a realistic dynamic representation of the system. The presence of damping, a force function of the relative velocity between the suspended and unsuspended masses, leads to undesirable dynamic behavior, as excessive damping suppresses the beneficial nonlinear motion of the mechanism, effectively preventing it from responding freely to impulsive excitations. The Design Study discussed earlier was repeated with a 50 mm

amplitude, varying C_v according to values of 0.6, 0.75, 0.85 Ns/m in the dMax and reference models [20], and plotting the trend in the frequency domain.

As seen in Figures 25 and 26, an increase in damping in both systems leads to a reduction in amplitude at resonance, potentially avoiding amplification. However, it also worsens performance at high frequencies, resulting in lower performance. Based on these analyses, a damping value of 0.75 Ns/m was chosen as it represents the minimum damping capable of improving performance by avoiding undesirable non-linear behaviors. This value is implemented in the curves shown in Figures 22–24. Following this, the performance of the three models under random-type forcing was evaluated; various road profiles were generated, among which one was selected. The Class E profile was implemented in MSC Adams® as a spline and used as a displacement motion applied to the wheel hub. Tests under this road profile were conducted at two velocities: 15 and 25 m/s. The attenuation of the three models under investigation was evaluated as the ratio between the RMS values of Chassis and Spindle Wheel accelerations. The results of these tests are shown in Figure 27.

It is worth noting that increasing damping improves vibration attenuation near resonance, contributing to enhanced ride comfort. However, excessive damping may adversely affect road holding by limiting the suspension's ability to follow high-frequency road irregularities. Therefore, an optimal damping value represents a compromise between comfort and handling performance.

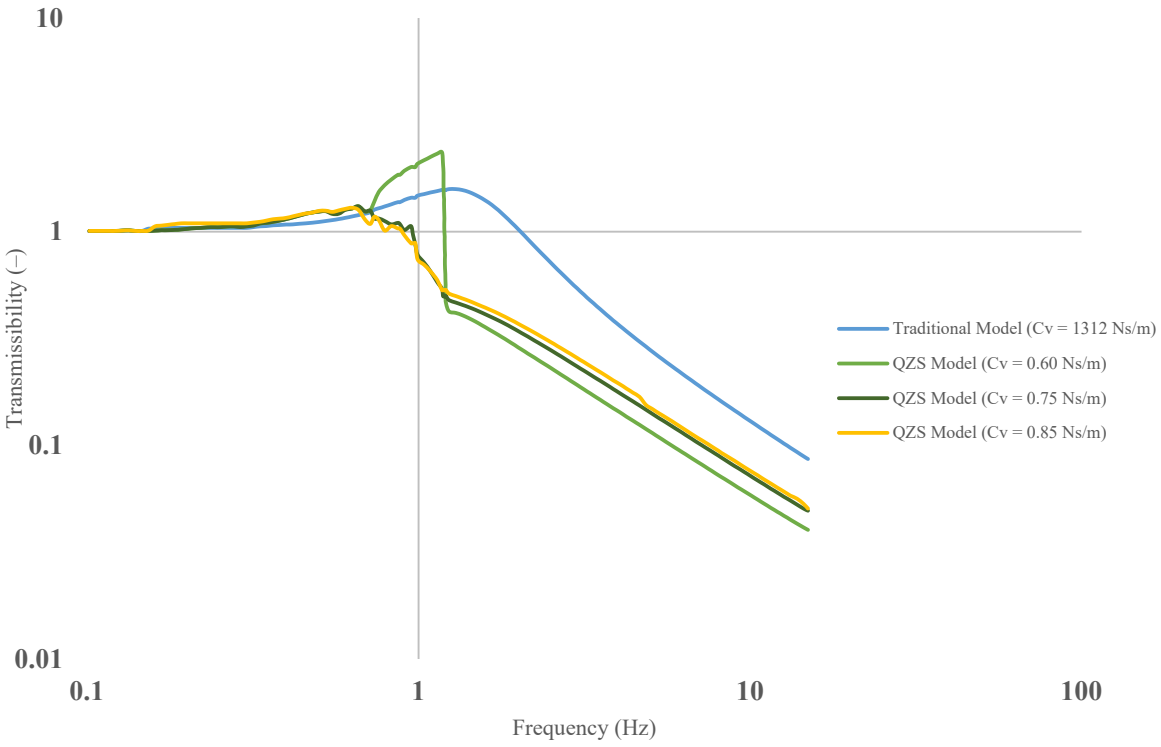

Figure 25. Influence of damping on the harmonic response of the Paper model.

From such analyses, it can be deduced that there is an actual improvement in isolation and/or comfort performance by the non-linear models compared to the traditional suspension. There is also a portion of the simulation under the road excitation of category E for the Traditional and dMax models, showing the time history of Chassis and Wheel shaking (Figures 28 and 29). Although the detailed frequency content cannot be directly observed from the time histories, they clearly show that the non-linear suspension exhibits smoother motion and reduced high-frequency oscillations compared to the Traditional model, which more directly follows the irregularities of the road profile.

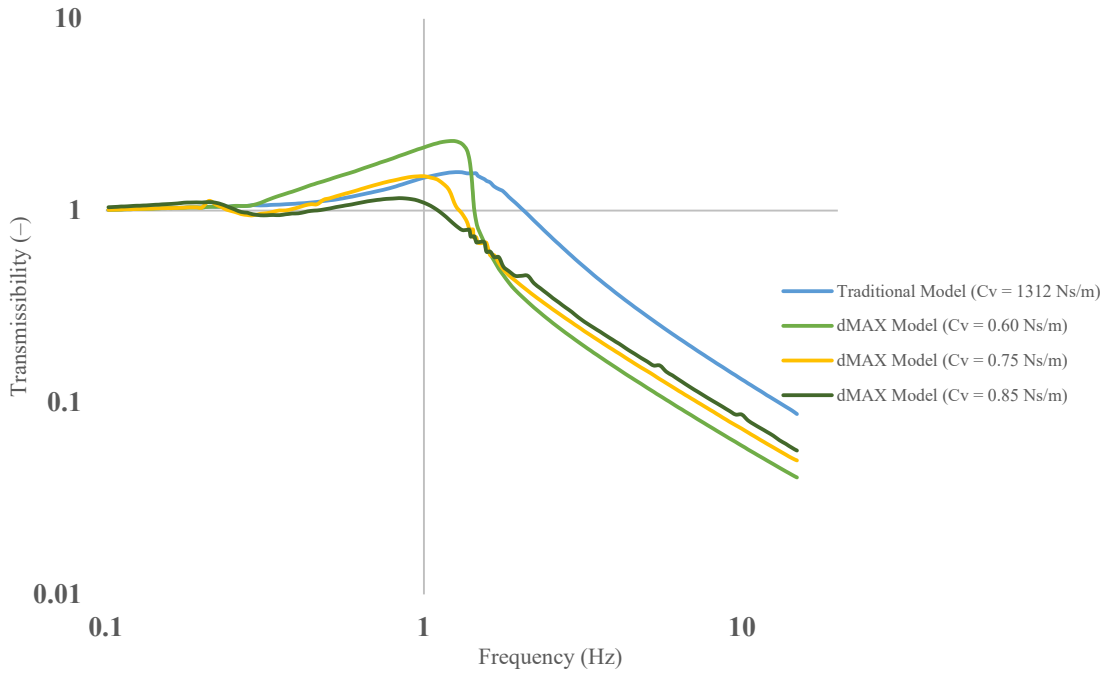

Figure 26. Influence of damping on the harmonic response of the dMax model.

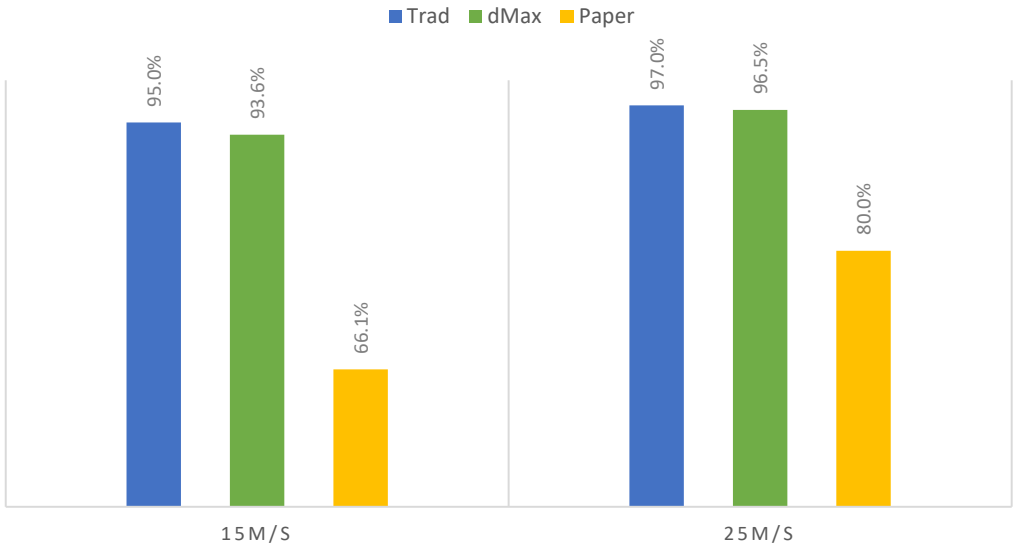

Figure 27. Acceleration attenuation under Category E Road profile simulation. The term attenuation refers to the RMS ratio $A_{\text{att}} = a_{\text{RMS, chassis}} / a_{\text{RMS, wheel}}$.

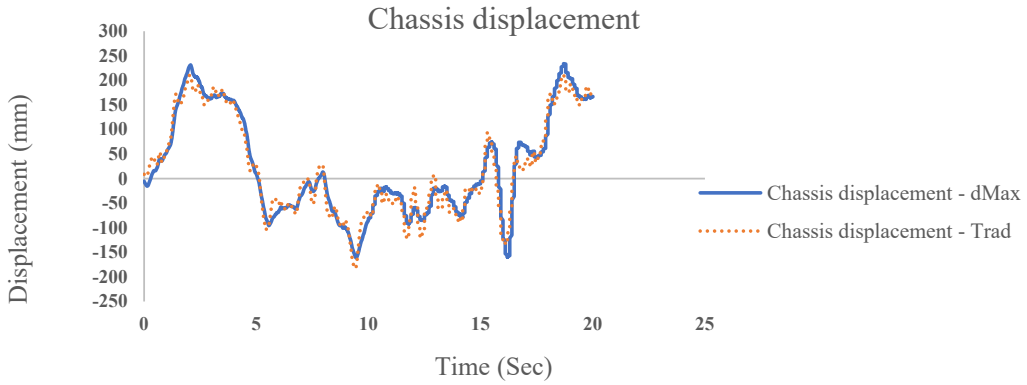

Figure 28. Comparison of Chassis vertical response for the Traditional and non-linear dMax suspension models under ISO 8608 Class E Road excitation at 15 m/s. Results obtained from MSC Adams® simulations.

Although Figure 29 presents a time history similar to that of the Traditional model (Figure 28), the dMax model shows slightly reduced peak-to-peak amplitudes and smoother oscillations, indicating a modest improvement in vibration isolation. The limited difference in the visual response can be attributed to the low excitation amplitude and the non-linear stiffness characteristics, which reduce the overall sensitivity of the system to road irregularities.

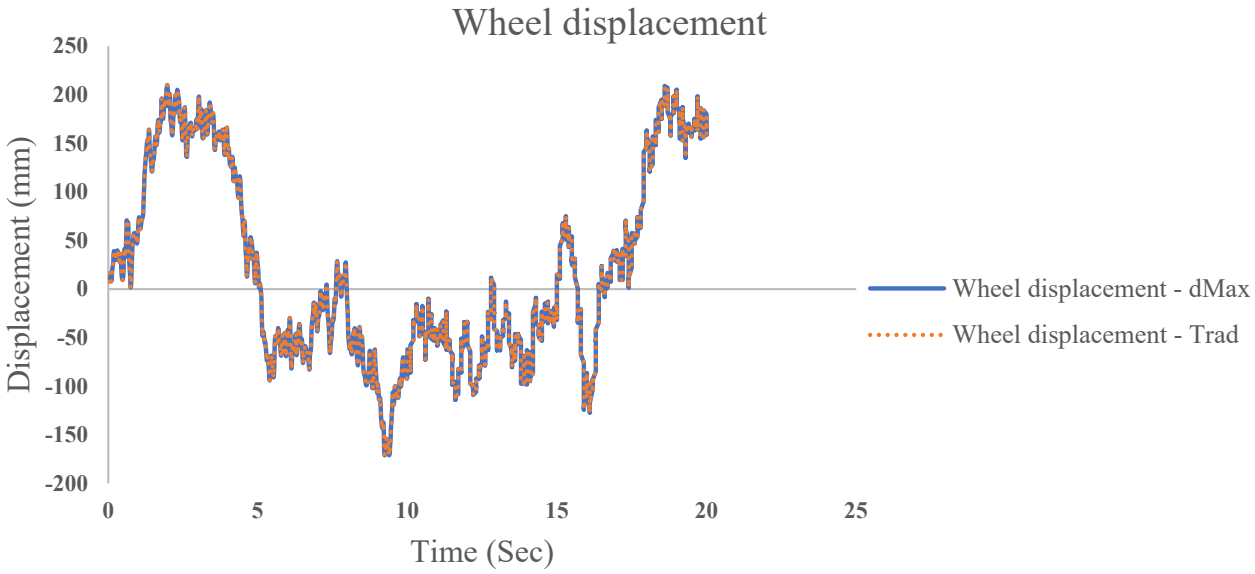

Figure 29. Comparison of wheel vertical response for the Traditional and non-linear dMax suspension models under ISO 8608 Class E Road excitation at 15 m/s. Results obtained from MSC Adams® simulations.

To better represent the positive aspects of the QZS suspension, an additional road profile was generated with a predominant harmonic content where QZS suspension performs better, between approximately 1 and 3.5 Hz. This was done to demonstrate the effective contribution of this type of suspension. Figure 30 shows the time histories for the Traditional model and Figure 31 for the non-linear dMax model. Simulations with this road profile yielded attenuation values in Figure 32.

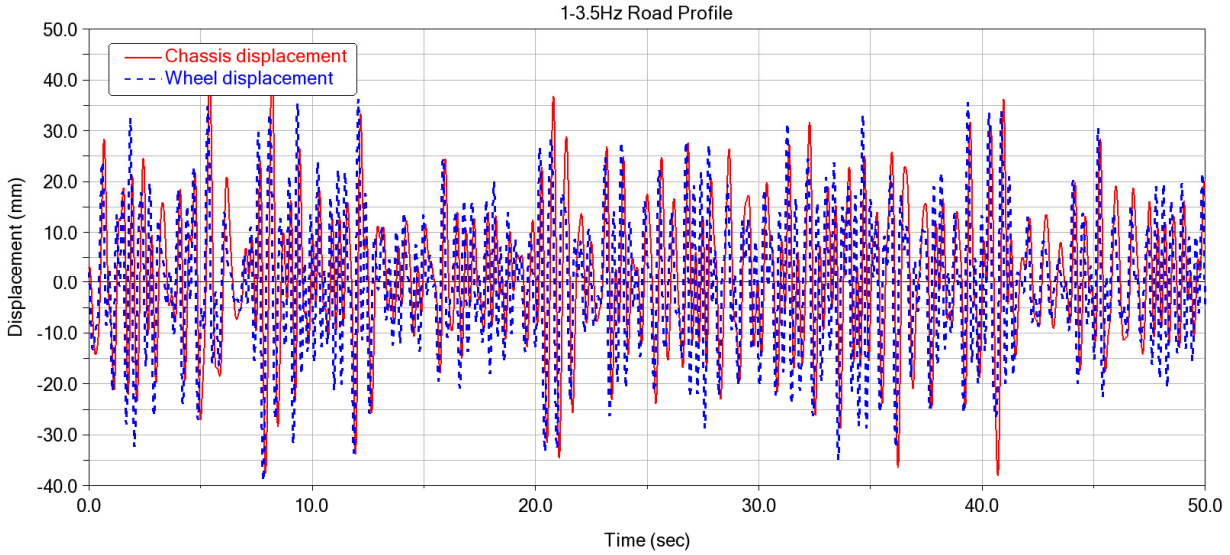

Figure 30. Time history analysis with road profile between 1 Hz and 3.5 Hz for the Traditional model. Results obtained from MSC Adams® simulations.

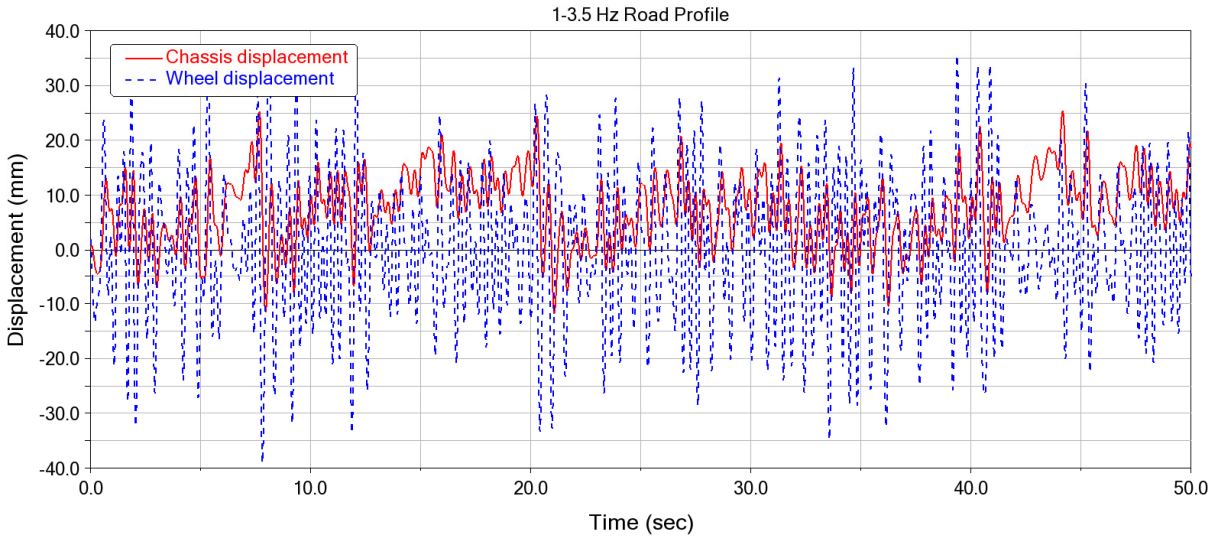

Figure 31. Time history analysis with road profile between 1 Hz and 3.5 Hz for the non-linear dMax model. Results obtained from MSC Adams® simulations.

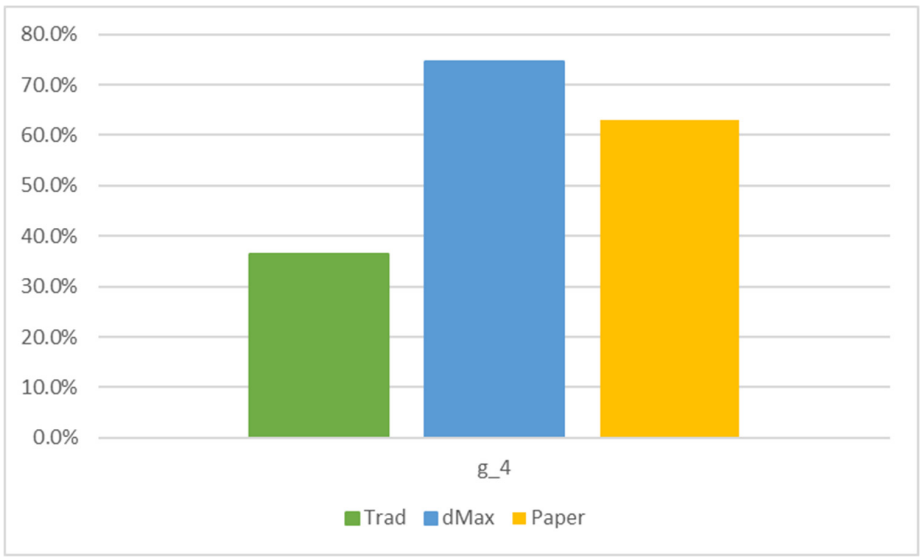

Figure 32. Attenuation of road profile with primary energy content between 1 Hz and 3.5 Hz.

This aspect is also well-represented by "Bump" simulations, a motion assimilated as impulsive, described by two cubic steps, one rising and one falling, each of 0.1 s with a constant section of 0.1 s in between. This type of excitation is characterized by more uniformly distributed harmonic contributions across the entire area of interest. As seen in Figure 33, these simulations better represent the benefits of the non-linear suspensions discussed so far. These models can attenuate 19% more than the Traditional model, going from 67% to 86%. It is noted that the attenuation level from Ref. [20], although comparable to the attenuation of the dMax model, does not fully represent the actual behavior. This parameterization leads to a static equilibrium problem where the mechanism does not return to the initial position after the bump excitation but stabilizes in a different configuration. This occurs because the geometric parameters of the model produce an asymmetric force–displacement relationship, causing an imbalance between the restoring forces during loading and unloading, and resulting in a shifted equilibrium point (see Figure 34). In contrast, it can be verified that the parameterization of the dMax model generates a correct behavior where the mechanism returns to the initial conditions (see Figure 35). The time history of the Bump simulations for the Traditional model is also shown in Figure 36.

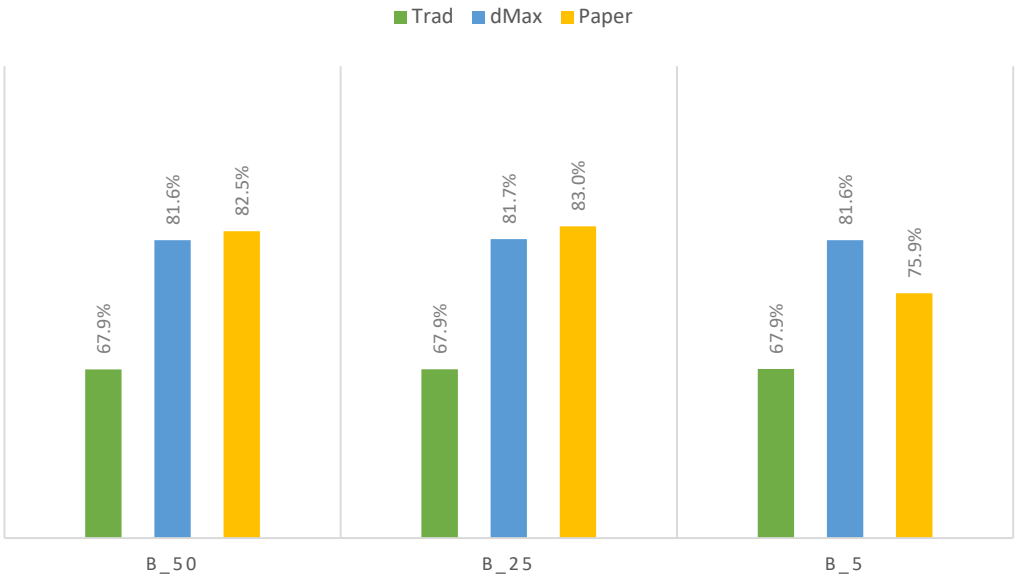

Figure 33. Acceleration attenuation under variable amplitude Bump simulation.

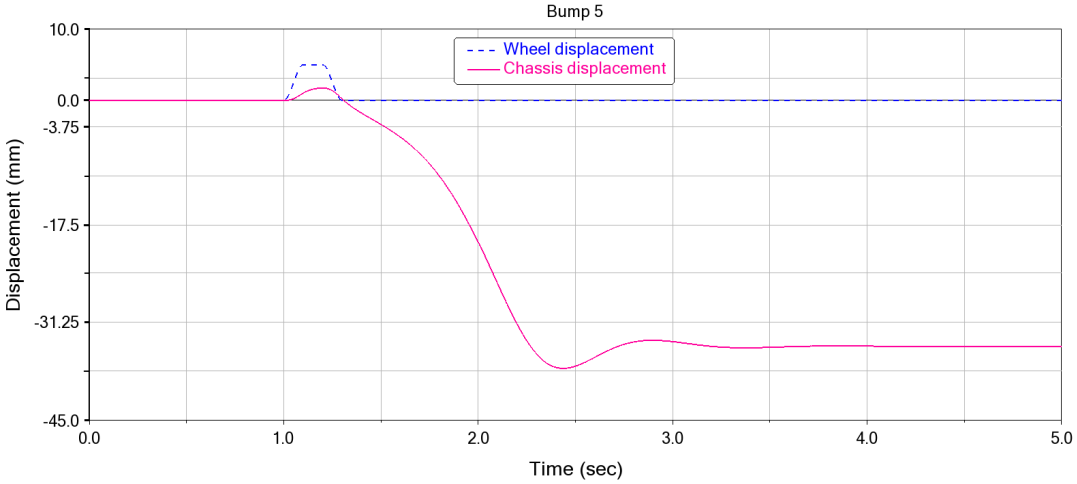

Figure 34. Bump simulation with amplitude 5, Reference model. Results obtained from MSC Adams® simulations.

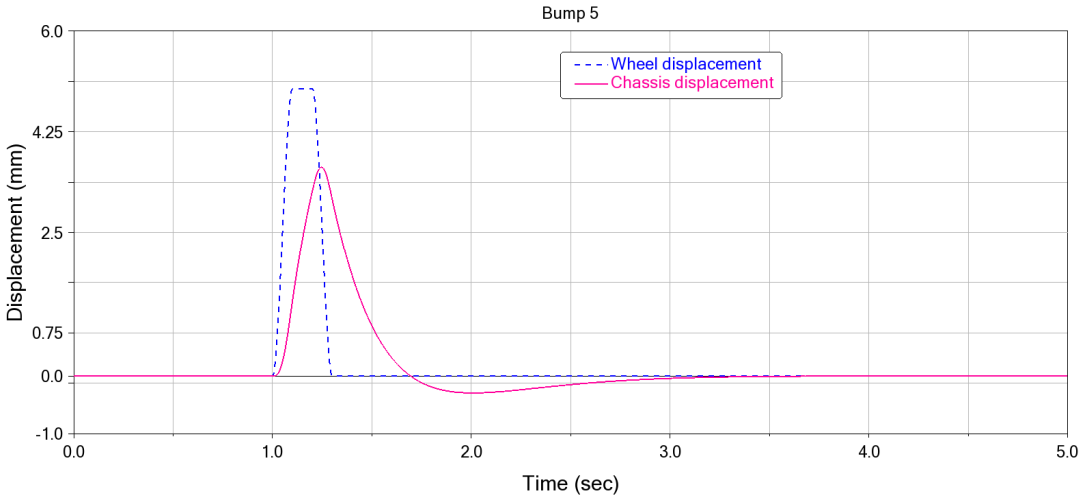

Figure 35. Bump simulation with amplitude 5, dMax model. Results obtained from MSC Adams® simulations.

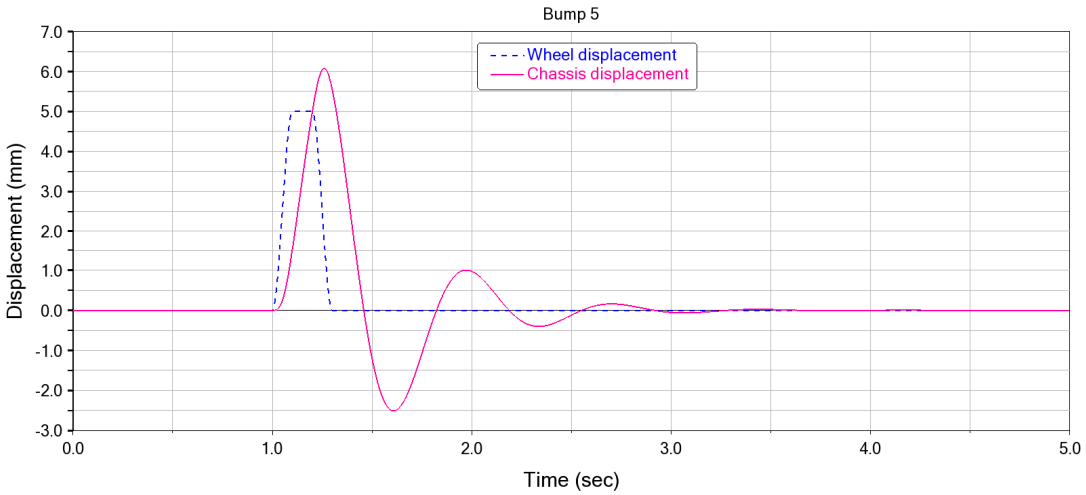

Figure 36. Bump simulation with amplitude 5, Traditional model. Results obtained from MSC Adams® simulations.

7. Conclusions

The application of a Quasi-Zero Stiffness suspension, specifically the "3 Springs" or "Oblique Springs" model, as the primary suspension of a vehicle, was analyzed. In this study, which focused on vertical dynamics and ride comfort, numerical simulations were conducted to demonstrate how this technology can lead to improved mechanical vibration isolation performance. The research objectives were successfully confirmed, and additional insights were obtained through a detailed multibody dynamics investigation. Overall, the critical aspects of this research focus on improving the transmissibility of the mechanism compared to a traditional suspension system. It was shown that this alternative solution can lead to a reduction in the natural frequency of the system (from approximately 1.3 Hz to about 1 Hz), a decrease in resonance transmissibility, and a mitigation of the trade-off between stiffness and static load-bearing capability. Consequently, improved attenuation performance is achieved in the low-frequency range, which is critical for driving comfort.

A critical point highlighted in this discussion concerns the theoretical scaling and parameterization of the non-linear system. Due to the intrinsic non-linearity of the suspension scheme, such parameterization may potentially lead to unstable configurations, as observed in the reference model reported in [20]. Future developments will therefore focus on scaling the suspension based on real commercial vehicle data and redesigning the system by introducing active functionalities to enhance adaptability under varying operating conditions. Furthermore, integrating the proposed suspension into Half-Car and Full-Car models represents an important extension of this work, enabling a more comprehensive evaluation in accordance with ISO 2631 standards and driving comfort criteria based on vehicle body motions such as pitch and roll. Finally, implementation within a Full-Car model would allow verification of the overall dynamic behavior under realistic driving conditions.

It should be noted that the present analysis focuses on the nominal performance of the suspension system under standardized road excitations. Although the system response is evaluated under different excitation amplitudes and road profiles, a systematic robustness assessment with respect to parametric uncertainties and extreme external disturbances is beyond the scope of this study and represents an important direction for future research.

The occurrence of slightly negative stiffness around the static equilibrium point, observed in some configurations, raises important safety considerations for real-world applications. In practical suspension systems, such conditions could potentially lead to local instability if not properly controlled. For this reason, the proposed design strategy

deliberately shifts the operating point toward configurations with a small but positive equivalent stiffness, ensuring static stability while preserving the beneficial quasi-zero stiffness behavior.

Moreover, the analysis highlights the inherent trade-off between ride comfort and road holding associated with damping selection. While lower damping values enhance vibration isolation and comfort, increased damping improves stability and road contact at the expense of high-frequency isolation. The selected damping configuration therefore represents a compromise between these competing requirements.

Despite the encouraging results obtained in this study, some limitations should be acknowledged. First, the analysis is entirely simulation-based and does not include experimental validation, which is necessary to fully assess the real-world applicability of the proposed suspension concept. Second, the vehicle is modeled using a simplified quarter car representation; therefore, full-vehicle dynamics such as pitch, roll, load transfer, and axle coupling effects are not captured. Moreover, the robustness of the proposed configuration with respect to parametric uncertainties (e.g., stiffness, damping, and mass variations) and severe or non-stationary external disturbances has not been investigated. Finally, the occurrence of quasi-zero or slightly negative stiffness is discussed from a theoretical perspective, while practical safety aspects and control strategies required for real-world implementation are beyond the scope of the present work.

Future work will focus on experimental validation of the proposed suspension concept, robustness analyses under parametric uncertainties and variable road excitations, and the extension of the methodology to semi-active and active suspension architectures.

In addition, ongoing research is focused on extending the proposed quasi-zero stiffness suspension concept to impulsive loading conditions and specific random vibration environments. In particular, the performance of the QZS mechanism under shock-type excitations and stochastic road-induced vibrations is currently being investigated to further evaluate its effectiveness in realistic and severe operating scenarios.

Author Contributions: Conceptualization, A.Z. and F.P.; Methodology, F.S.S., A.M., A.Z. and F.P.; Software, A.Z.; Validation, A.Z. and F.P.; Formal analysis, F.S.S., A.M., A.Z. and F.P.; Investigation, F.S.S., A.M., A.Z. and F.P.; Resources, A.Z. and F.P.; Data curation, A.Z.; Writing—original draft, F.S.S., A.M., A.Z. and F.P.; Writing—review & editing, F.S.S., A.M., A.Z. and F.P.; Visualization, F.S.S., A.M., A.Z. and F.P.; Supervision, A.Z. and F.P.; Project administration, A.Z. and F.P.; Funding acquisition, A.Z. and F.P. All authors have read and agreed to the published version of the manuscript.

Funding: This research was funded by the NA TO Science for Peace and Security (SPS) Programme (grant number G6176).

Data Availability Statement: Data are contained within the article.

Conflicts of Interest: The authors declare no conflict of interest.

List of Symbols

Symbol	Description
a	Half distance between oblique spring attachment points
h_0	Static deflection of the suspension
L_0	Rest length of the oblique springs
x	Vertical displacement
$\hat{x} = x/L_0$	Dimensionless displacement
θ	Initial angle of oblique springs
$\gamma = a/L_0 = \cos\theta$	Geometric parameter
k_v	Vertical spring stiffness
k_h	Horizontal/oblique spring stiffness

$\alpha = K_v/K_h$	Stiffness ratio
f	Force of the suspension
$\hat{f}$	Dimensionless force
f_{adim}	A dimensional (dimensionless) force—equivalent to $\hat{f}$
K	Equivalent stiffness
$\hat{K}$	Dimensionless stiffness
P_v	Preload of the vertical spring
P_h	Preload of the oblique springs
m	Sprung mass (Chassis)
m_n	Unsprung mass (wheel group)
m_{eq}	Equivalent mass
C_v	Suspension damping coefficient
C_{eq}	Equivalent damping coefficient
ζ	Damping ratio
$z(t)$	Displacement of sprung mass
$y(t)$	Displacement of unsprung mass
$\dot{z},\ \dot{y}$	Velocities of sprung and unsprung masses
$\ddot{z}, \ddot{y}$	Accelerations of sprung and unsprung masses
δ	Relative suspension deflection (between sprung and unsprung mass)
Z, Y	Amplitudes of harmonic responses
ϕ, ψ	Phase angles of harmonic responses
Ω	Excitation frequency (rad/s)
Ω_n	Natural frequency of the system
$r = \Omega/\Omega_n$	Frequency ratio
T	Transmissibility (force/displacement ratio)
d	Suspension travel around the equilibrium
$\hat{d}$	Dimensionless suspension travel
$z_r(x)$	Road profile function
L	Total road length
Δn	Frequency increment for road profile
n_0	Base spatial frequency (0.1 m^{-1})
n_i	i^{th} spatial frequency
ϕ_i	Random phase angle of i^{th} harmonic
k	ISO road class exponent
σ	Spectral density parameter in the road roughness model
$G_d(n)$	Power Spectral Density (PSD) of road profile, as defined in ISO 8608
E	Young's modulus
I	Second moment of area of the beam
k_b	Stiffness of buckled beam ($k_b = \pi^2 EI/L^2$)
F_n	Normal dynamic load on the driven gear or spring system
F_z	Vertical dynamic force component
P_w, P_{sl}, P_{la}	Loads in the static balance of the Lower Arm
M_{w}	Moment of wheel load

List of Abbreviations

Abbreviation	**Description**
QZS	Quasi-Zero Stiffness
DOF	Degree of Freedom
RMS	Root Mean Square
ISO	International Organization for Standardization
MATLAB	Matrix Laboratory—Numerical computing environment
MSC ADAMS	Automated Dynamic Analysis of Mechanical Systems—Multibody simulation software

CV	Constant Value
DV	Design Variable

References

1. Rao, S.S. *Mechanical Vibrations*, 6th ed.; Pearson Education: Upper Saddle River, NJ, USA, 2017.
2. Brennan, M.J.; Kovacic, I.; Carrella, A.; Waters, T.P. On the Jump-Up and Jump-Down Frequencies of the Duffing Oscillator. *J. Sound Vib.* **2008**, *318*, 1250–1261. [CrossRef]
3. Carrella, A.; Brennan, M.J.; Waters, T.P. Static Analysis of a Passive Vibration Isolator with Quasi-Zero-Stiffness Characteristic. *J. Sound Vib.* **2007**, *301*, 678–689. [CrossRef]
4. Zhao, F.; Ji, J.; Ye, K.; Luo, Q. An Innovative Quasi-Zero Stiffness Isolator with Three Pairs of Oblique Springs. *Int. J. Mech. Sci.* **2021**, *192*, 106093. [CrossRef]
5. Lan, C.C.; Yang, S.A.; Wu, Y.S. Design and Experiment of a Compact Quasi-Zero-Stiffness Isolator Capable of a Wide Range of Loads. *J. Sound Vib.* **2014**, *333*, 4843–4858. [CrossRef]
6. Danh, L.T.; Ahn, K.K. Active Pneumatic Vibration Isolation System Using Negative Stiffness Structures for a Vehicle Seat. *J. Sound Vib.* **2014**, *333*, 1245–1268. [CrossRef]
7. Ye, K.; Ji, J. An Origami-Inspired Quasi-Zero Stiffness Vibration Isolator Using a Novel Truss–Spring-Based Stack Miura-Ori Structure. *Mech. Syst. Signal Process.* **2022**, *165*, 108383. [CrossRef]
8. Liu, X.; Huang, X.; Hua, H. On the Characteristics of a Quasi-Zero Stiffness Isolator Using Euler Buckled Beam as Negative Stiffness Corrector. *J. Sound Vib.* **2013**, *332*, 3359–3376. [CrossRef]
9. Huang, X.; Liu, X.; Sun, J.; Zhang, Z.; Hua, H. Vibration Isolation Characteristics of a Nonlinear Isolator Using Euler Buckled Beam as Negative Stiffness Corrector: A Theoretical and Experimental Study. *J. Sound Vib.* **2014**, *333*, 1132–1148. [CrossRef]
10. Zhou, J.; Wang, X.; Xu, D.; Bishop, S. Nonlinear Dynamic Characteristics of a Quasi-Zero Stiffness Vibration Isolator with Cam–Roller–Spring Mechanisms. *J. Sound Vib.* **2015**, *346*, 53–69. [CrossRef]
11. Zhou, J.; Xiao, Q.; Xu, D.; Ouyang, H.; Li, Y. A Novel Quasi-Zero-Stiffness Strut and Its Applications in Six-Degree-of-Freedom Vibration Isolation Platform. *J. Sound Vib.* **2017**, *394*, 59–74. [CrossRef]
12. Zhou, J.; Xu, D.; Bishop, S. A Torsion Quasi-Zero Stiffness Vibration Isolator. *J. Sound Vib.* **2015**, *338*, 121–133. [CrossRef]
13. Shan, Y.; Wu, W.; Chen, X. Design of a Miniaturized Pneumatic Vibration Isolator with High-Static–Low-Dynamic Stiffness. *J. Vib. Acoust.* **2015**, *137*, 045001. [CrossRef]
14. Zheng, Y.; Zhang, X.; Luo, Y.; Yan, B.; Ma, C. Design and Experiment of a High-Static–Low-Dynamic Stiffness Isolator Using a Negative Stiffness Magnetic Spring. *J. Sound Vib.* **2016**, *360*, 31–52. [CrossRef]
15. Zhou, J.; Wang, K.; Xu, D.; Ouyang, H.; Li, Y. A Six Degrees-of-Freedom Vibration Isolation Platform Supported by a Hexapod of Quasi-Zero-Stiffness Struts. *J. Vib. Acoust.* **2017**, *139*, 034502. [CrossRef]
16. Dai, H.; Jing, X.; Sun, C.; Wang, Y.; Yue, X. Accurate Modeling and Analysis of a Bio-Inspired Isolation System with Application to On-Orbit Capture. *Mech. Syst. Signal Process.* **2018**, *109*, 111–133. [CrossRef]
17. Sun, X.; Xu, J.; Wang, F.; Zhang, S. A Novel Isolation Structure with Flexible Joints for Impact and Ultralow-Frequency Excitations. *Int. J. Mech. Sci.* **2018**, *146–147*, 366–376. [CrossRef]
18. Deng, T.; Wen, G.; Ding, H.; Lu, Z.Q.; Chen, L.Q. A Bio-Inspired Isolator Based on Characteristics of Quasi-Zero Stiffness and Bird Multi-Layer Neck. *Mech. Syst. Signal Process.* **2020**, *145*, 106967. [CrossRef]
19. Wu, Z.; Jing, X.; Bian, J.; Li, F.; Allen, R. Vibration Isolation by Exploring Bio-Inspired Structural Nonlinearity. *Bioinspir. Biomim.* **2015**, *10*, 056015. [CrossRef]
20. Suman, S.; Balaji, P.S.; Selvakumar, K.; Kumaraswamidhas, L.A. Nonlinear Vibration Control Device for a Vehicle Suspension Using Negative Stiffness Mechanism. *SN Appl. Sci.* **2021**, *3*, 957. [CrossRef]
21. Saini, M. Modelling and Simulation of Vehicle Suspension System with Variable Stiffness Using Quasi-Zero Stiffness Mechanism. *SAE Int. J. Veh. Dyn. Stab. NVH* **2020**, *4*, 37–47. [CrossRef]
22. Barbieri, M.; Ilanko, S.; Pellicano, F. Active Vibration Control of Seismic Excitation. *Nonlinear Dyn.* **2018**, *93*, 41–52. [CrossRef]
23. Zippo, A.; Ferrari, G.; Amabili, M.; Barbieri, M.; Pellicano, F. Active Vibration Control of a Composite Sandwich Plate. *Compos. Struct.* **2015**, *128*, 100–114. [CrossRef]
24. Parvez, Y.; Chauhan, N.R.; Srivastava, M. Vibration Control and Comparative Analysis of Passive and Active Suspension Systems Using PID Controller with Particle Swarm Optimization. *J. Inst. Eng. Ser. C* **2025**, *106*, 1–19. [CrossRef]
25. Abut, T.; Salkim, E.; Tugal, H. Active Suspension Control for Improved Ride Comfort and Vehicle Performance Using HHO-Based Type-I and Type-II Fuzzy Logic. *Biomimetics* **2025**, *10*, 673. [CrossRef] [PubMed]
26. Li, Q.; Chen, Z.; Song, H.; Dong, Y. Model Predictive Control for Speed-Dependent Active Suspension System with Road Preview Information. *Sensors* **2024**, *24*, 2255. [CrossRef]
27. Zhao, Z.; Wang, C.; Zhao, J.; Du, W. LQR Force Command Planning–Based Sliding Mode Control for Active Suspension System. *Proc. Inst. Mech. Eng. Part I—J. Syst. Control Eng.* **2024**, *238*, 373–385. [CrossRef]

28. Saber, H.; Samani, F.S.; Pellicano, F. Nonlinear Vibration Absorbers Applied on Footbridges. *Meccanica* **2021**, *56*, 23–40. [CrossRef]
29. Saber, H.; Samani, F.S.; Pellicano, F. Vibration Reduction of Footbridges Subjected to Walking, Running, and Jumping Pedestrian Loads. *J. Vib. Control* **2022**, *29*, 3227–3240. [CrossRef]
30. Saber, H.; Samani, F.S.; Pellicano, F. A Novel Nonlinear Variable Damping Device and Its Application for Systems with Uncertain Parameters. *Proc. Inst. Mech. Eng. Part K—J. Multi-Body Dyn.* **2022**, *236*, 660–671. [CrossRef]
31. Liu, C.; Chen, L.; Lee, H.P.; Yang, Y.; Zhang, X. A Review of the Inerter and Inerter-Based Vibration Isolation: Theory, Devices, and Applications. *J. Frankl. Inst.* **2022**, *359*, 10671–10709. [CrossRef]
32. Eskandary-Malayery, F.; Ilanko, S.; Mace, B.; Mochida, Y.; Pellicano, F. Experimental and Numerical Investigation of a Vertical Vibration Isolator for Seismic Applications. *Nonlinear Dyn.* **2022**, *109*, 303–322. [CrossRef]
33. Iarriccio, G.; Zippo, A.; Eskandary-Malayery, F.; Ilanko, S.; Mochida, Y.; Mace, B.; Pellicano, F. Tunable High-Static-Low-Dynamic Stiffness Isolator under Harmonic and Seismic Loads. *Vibration* **2024**, *7*, 829–843. [CrossRef]
34. Zippo, A.; Iarriccio, G.; Molaie, M.; Pellicano, F. Novel Nonlinear Suspension Based on Concept of Origami Metastructures: Theoretical and Experimental Investigations. *Vibration* **2024**, *7*, 1126–1155. [CrossRef]
35. Molaie, M.; Deylaghian, S.; Iarriccio, G.; Samani, F.S.; Zippo, A.; Pellicano, F. Planet Load-Sharing and Phasing. *Machines* **2022**, *10*, 634. [CrossRef]
36. Sui, G.; Zhang, X.; Hou, S.; Shan, X.; Hou, W.; Li, J. Quasi-Zero Stiffness Isolator Suitable for Low-Frequency Vibration. *Machines* **2023**, *11*, 512. [CrossRef]
37. Zhang, L.; Zhao, C.; Qian, F.; Dhupia, J.; Wu, M. A Variable Parameter Ambient Vibration Control Method Based on Quasi-Zero Stiffness in Robotic Drilling Systems. *Machines* **2021**, *9*, 67. [CrossRef]
38. Ma, Z.; Zhou, R.; Yang, Q. Recent Advances in Quasi-Zero Stiffness Vibration Isolation Systems: An Overview and Future Possibilities. *Machines* **2022**, *10*, 813. [CrossRef]
39. Zhu, Z.; Li, Y. Biomimetic Nonlinear X-Shaped Vibration Isolation System for Jacket Offshore Platforms. *Machines* **2025**, *13*, 998. [CrossRef]
40. Zhang, L.; Zhao, C.; Qian, F.; Dhupia, J.; Wu, M. An Active Control with a Magnetorheological Damper for Ambient Vibration. *Machines* **2022**, *10*, 82. [CrossRef]
41. Norton, R.L. *Design of Machinery*; McGraw-Hill: Columbus, OH, USA, 2019.
42. Adams Tutorial Kit for Mechanical Engineering Courses. Available online: https://hexagon.com/resources/resource-library/adams-tutorial-kit-mechanical-engineering-courses (accessed on 2 February 2026).
43. Guiggiani, M. *The Science of Vehicle Dynamics: Handling, Braking, and Ride of Road and Race Cars*; Springer: Dordrecht, The Netherlands, 2014. [CrossRef]
44. Pellicano, F. *Mechanical Vibrations*; Independently Published: Chicago, IL, USA, 2025.
45. Múčka, P. Simulated Road Profiles According to ISO 8608 in Vibration Analysis. *J. Test. Eval.* **2017**, *46*, 20160265. [CrossRef]
46. Agostinacchio, M.; Ciampa, D.; Olita, S. The Vibrations Induced by Surface Irregularities in Road Pavements—A MATLAB® Approach. *Eur. Transp. Res. Rev.* **2014**, *6*, 267–275. [CrossRef]